Structure of late Variscan Millevaches leucogranite massif in the French Massif Central: AMS and gravity modelling results.

Aude Gébelin, Guillaume Martelet, Yan Chen, Maurice Brunel, Michel Faure

Structure of late Variscan Millevaches leucogranite massif in the French Massif Central: AMS and gravity modelling results

Aude Gébelin[a], Guillaume Martelet[b], Yan Chen[c], Maurice Brunel[a] and Michel Faure[c]

[a]Laboratoire Dynamique de la Lithosphère, Université Montpellier II, CC060, Place E. Bataillon, 34095 cedex 5, Montpellier, France
[b]BRGM, BP 6009, 45060 Orléans cedex, France
[c]Institut des Sciences de la Terre d'Orléans, UMR 6113, Université d'Orléans, BP 6759, 45067 Orléans cedex 2, France

Abstract

In the Limousin area, Variscan leucogranitic plutons are spatially associated with normal faults and major strike-slip shear zones that are a continuation of the South Armorican shear zone. Our study focuses on the large N–S-trending Millevaches granitic massif (Massif Central, France), and intends to highlight, through gravity modelling, structural and anisotropy of magnetic susceptibility (AMS), the massif structure at depth and to discuss the mode of emplacement of granites within a strike-slip tectonic context. The mica subfabric suggests that the magnetic foliations display a general NW–SE sub-horizontal pattern on both sides of the N–S Pradines dextral wrench fault zone that deforms the core of the massif on 5 km width. The magnetic lineation trend exhibits a sigmoïdal pattern, N–S in the Pradines fault zone and NW–SE on both sides of it, which are consistent with a dextral wrench component. The horizontal magnetic foliations and lineations are consistent with the thin granite laccolith model. There is no significant imprint of the extensional Variscan belt collapse on the internal fabric of Millevaches granites than the tectonic dextral transcurrent movement prevailing in this area.

Keywords: AMS; Gravity; Shear zone; Granitic pluton; French Massif Central; Millevaches

1. Introduction

Granitic magmatism constitutes one of the main processes of material and heat transfer in the continental crust. In the Massif Central, granites form nearly 50% of the ante-stephanian surface outcrops. The mechanisms of emplacement and the deformation of granites provide information on the processes of continental crustal evolution. In the Limousin area (northwestern part of the Variscan French Massif Central), leucogranite emplacement is interpreted as related to Carboniferous post-collisional thinning during a NW–SE-trending ductile deformation (Faure, 1989 and Faure and Pons, 1991). The leucogranitic intrusions are spatially associated with normal faults and major strike-slip shear zones that are a continuation of the South Armorican shear zone. Many studies (Tikoff and Saint Blanquat, 1997, Brown and Solar, 1998 and Koukouvelas et al., 2002) emphasize close relationships between faults and plutonism in various tectonic contexts (magmatic arc, continental collision zone, etc.). In the last few years, Speer et al., 1994 and Ingram and Hutton, 1994 have

proposed that shear zones could play a role in the transport and emplacement of magmas within the crust. There is still current debate about how tectonic movements along shear zones control the mechanisms of transport, ascent, and emplacement of magmas.

This paper documents the relationships between major faults and granites in the Millevaches massif (Massif Central, France). The granitic body is located in the Limousin region and is particularly unusual because it has a N–S tectonic trend rather than the usual E–W to NW–SE trend of the Variscan belt. The Millevaches granite massif is affected by large ductile shear zones, which may have played a role in magma emplacement. In this study, we will address several problems: Did shear zones play a significant role in magma transport and magma emplacement? Did they have an impact on the internal fabric of granites? Did magma rheology influence the location of the crustal deformation? What is the relative chronology between magma emplacement, regional tectonics, and ductile shear zones? To answer these questions we used structural geology, anisotropy of magnetic susceptibility (AMS) and gravity modelling. The structural observations provide information on the granite fabrics at the scale of massif and on the granite deformation in relation to ductile shear zones. Hutton, 1982 and Courrioux, 1983 document relationships between the pluton's internal fabric, geometry and kinematics of shear zones. Our study complements previously published structural and AMS data in the northern part of the massif (Jover, 1986), with new data in the central and south part of the massif. Finally, to highlight the massif structure at depth, gravity modelling has been performed throughout the massif.

2. Geological setting

2.1. Regional framework

The study area belongs to the northwestern part of the Variscan Massif Central, in France (Fig. 1). The Limousin region is located to the west of the Sillon Houiller sinistral wrench fault, and is characterised by numerous leucogranitic plutons related to the Variscan orogeny.

The timing of Variscan orogeny in the Massif Central ranges from Late Silurian time, corresponding to the HP–MT metamorphic event, to late Carboniferous–early Permian that marks the end of the late-orogenic sedimentation (Matte, 1998). Crustal thickening was achieved by south-verging deep-seated metamorphic nappes associated with high-pressure metamorphism and crustal melting (Matte, 1986 and Ledru et al., 1989). The Variscan Massif Central experienced two successive stages of extension from Middle Carboniferous to Early Permian (Faure, 1995). In the Limousin region, the first one began in the late Visean and is marked by the Namuro-Wesphalian (330–315 Ma) emplacement of synkinematic leucogranites that recorded a NW–SE stretching lineation (Faure, 1995). The second extensional stage occurred from Late Carboniferous to Early Permian and is characterised by NE–SW stretching. Late Variscan times corresponded to the development of dextral and sinistral ductile wrench faults (Arthaud and Matte, 1977). The dextral South Armorican shear zone is one of these shear zones that could be responsible for the emplacement of biotite-muscovite granites (Guineberteau et al., 1987) dated at ca. 320 Ma (Vidal, 1973). It is possible that the South Armorican shear zone could continue into the Limousin region (Colchen and Rolin, 1996).

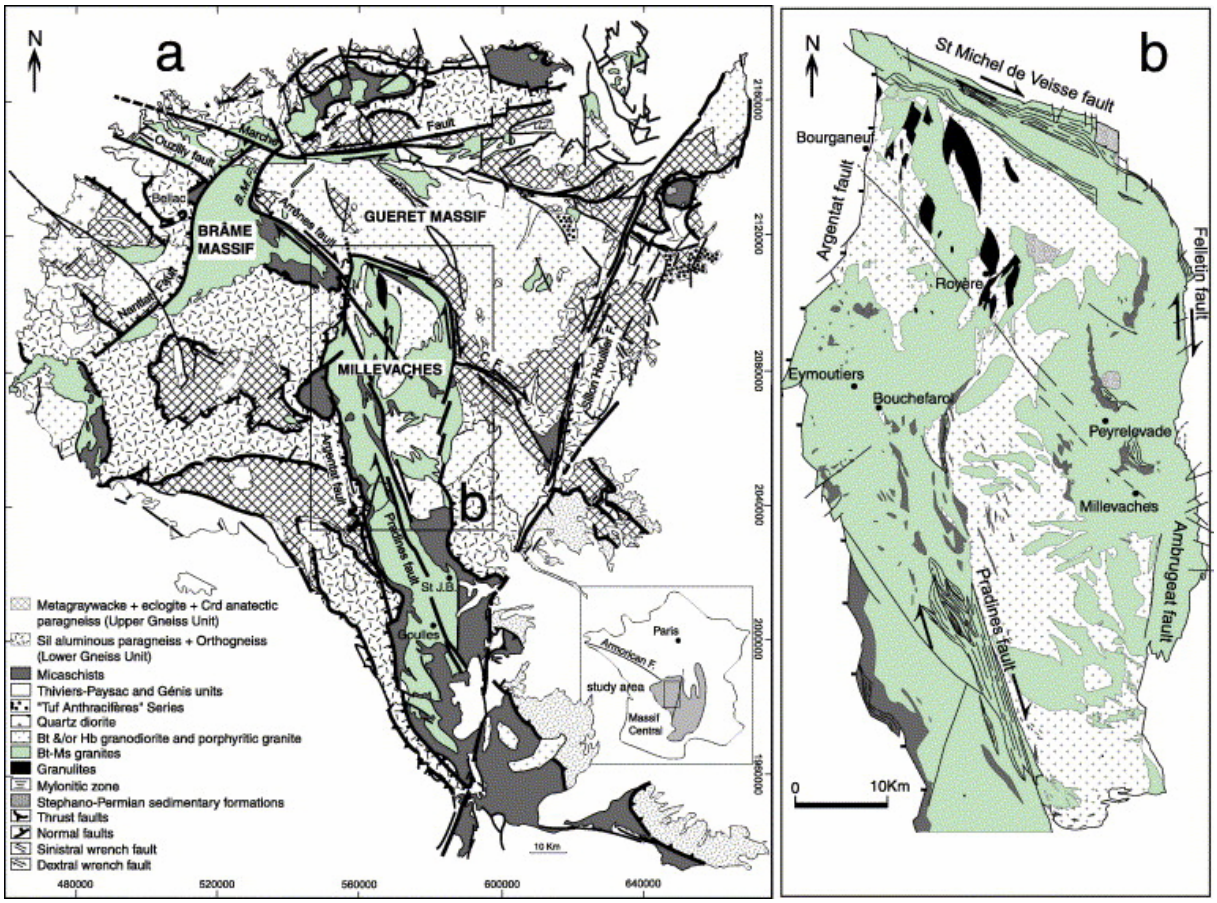

Fig. 1. Simplified geological map of the northwestern part of the Massif Central, France. (a) Structural map of the study area in the French Massif Central. (b) Millevaches massif lithologic units map.

The Limousin structural map is characterised by a series of E–W and NW–SE striking wrench faults such as the E–W Marche sinistral wrench fault and the NW–SE Ouzilly, Arrênes, St Michel de Veisse (St M.V.F.), Felletin (F.F.) and La Courtine (C.F.) dextral wrench faults (Fig. 1a). As in the Armorican massif, these faults have the same strike and all of them have close spatial relationships with leucogranites. In the Limousin region, normal faults cut these strike-slip faults at right angles. From west to east, we recognize the Nantiat normal fault, which forms the west boundary of the Brâme leucogranites and separates them from the Bellac Paleozoïc units, and the Bussières-Madeleine normal fault (B.-M.F.) that separates the Brâme massif from the Guéret massif in the east (Fig. 1a). The Argentat normal fault defines the western boundary of the Millevaches massif (Fig. 1a and b).

2.2. The Millevaches massif

The Millevaches massif is limited to the west by the ductile and brittle Argentat normal fault, which separates it from the Limousin metamorphic units (Floc'h, 1983) (Fig. 1a). To the north, the St Michel de Veisse dextral wrench fault (St.M.V.F.) separates the Millevaches and Guéret Massifs (Fig. 1a). Finally to the east, the boundary with cordierite anatectic and biotite-sillimanite paragneiss units corresponds to the Felletin fault (F.F., Fig. 1a) shear zone (Fig. 1b), which continues southward as the Ambrugeat fault (Fig. 1b). The wide (5 km) and N–S striking Pradines ductile dextral wrench fault cuts the Millevaches massif in its centre (Fig. 1a and b).

The Millevaches massif (Fig. 1b) consists of several plutons of porphyritic biotite granite and two-mica leucogranite intruded into micaschists known as the Para-autochthonous Unit (Ledru et al., 1989). Two-mica leucogranites derive from partial melting of metasediments (Cuney et al., 1990 and Williamson et al., 1996) whereas, according to Downes et al. (1997), the porphyritic biotite granites come from the mixing of mantle and crustal magmas. The micaschist and granite foliations are concordant. In the Pradines fault, the granite and micaschist foliations strike NNW–SSE and present a high dip (>55°) (Fig. 2a). Micaschists underwent a bed by bed partial melting during the Pradines dextral wrench fault activity (Fig. 2b). On both sides of the Pradines fault, the micaschist foliations are sub-horizontal (Fig. 2c). They endured a partial melting event (Fig. 2c), which produced the two-mica leucogranites with sub horizontal foliation (Fig. 2d). In the north part of the Pradines dextral wrench fault, the micaschists experienced a granulitic metamorphism. The granulites are formed of two rock types (Fig. 1b): a paleosome at biotite–cordierite–garnet–sillimanite and a leucosome that looks like garnet–cordierite leucogranite. In the N–S Argentat normal fault zone, the granite and micaschist foliations strike NW–SE with a variable dip between 35 and 65° west. In the trending E–W to NW–SE St Michel de Veisse dextral wrench fault, micaschists outcrop along the boundary fault or as xenoliths within granites. In Felletin-La Courtine and Ambrugeat dextral wrench faults, the granite foliation dips vertically and strikes N–S.

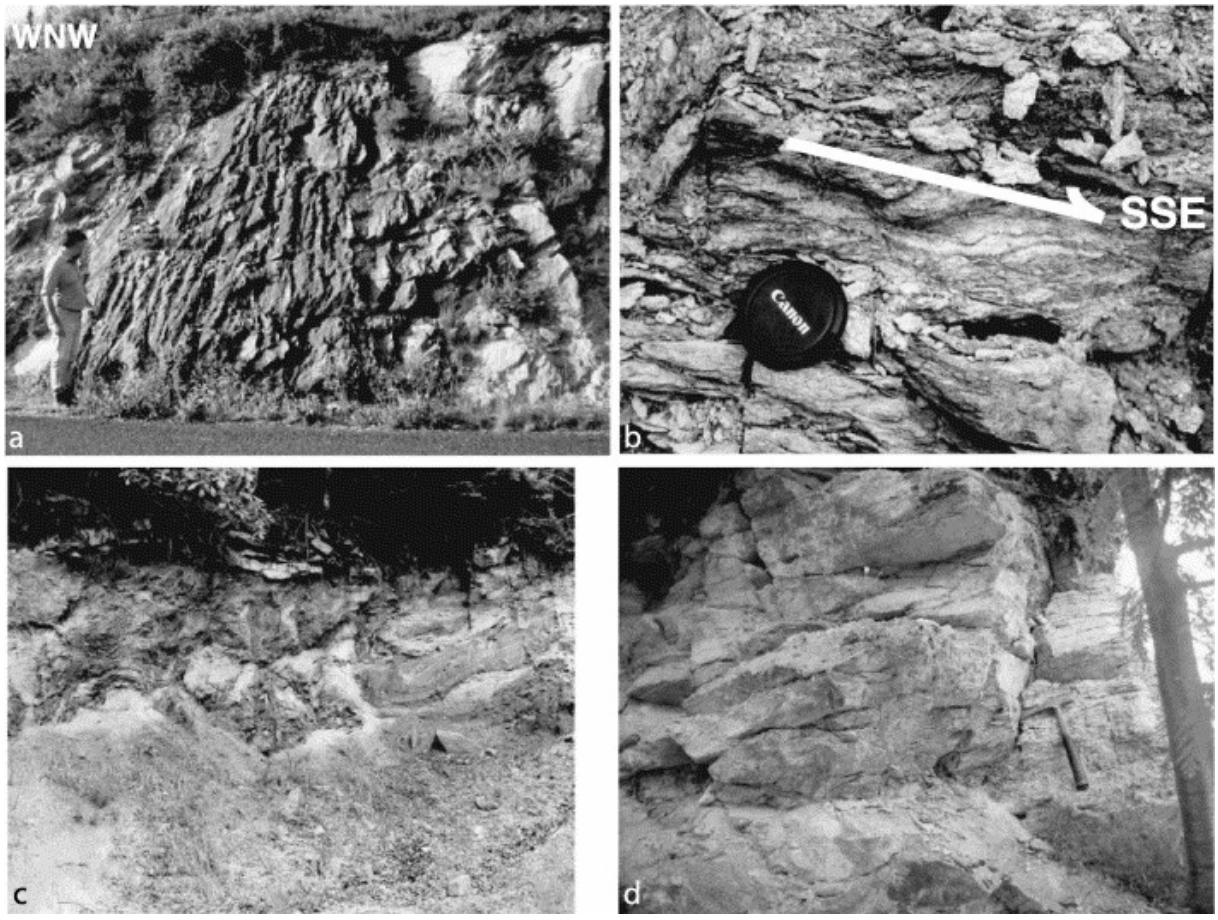

Fig. 2. Field photographs of Millevaches two-mica leucogranites and wall rocks. (a) Granites high dip foliation in the Pradines fault. (b) Micaschists suffered a bed by bed partial melting during the Pradines dextral wrench fault activity. (c) Sub horizontal foliation micaschists experienced the partial melting event. (d) Granites sub horizontal foliation on both sides of the Pradines fault.

It is difficult to establish exactly the timing of the emplacement of the various rock types because isotopic data are very scarce or questionable. Available Rb/Sr ages for the leucogranites of the south part of the Millevaches, based on whole rock analysis, yielded an age of 332±6 Ma in the Goulles leucogranite (Fig. 1a), and 336±7 Ma in the St Julien-aux-Bois leucogranite (St J.B.) (Fig. 1a) (Monier, 1980). The Bouchefarol porphyritic-biotite granite (Fig. 1b) gives an age of 357±7 Ma (Augay, 1979) and the garnet–cordierite leucogranite (granulites, Fig. 1b) has an age of 332±15 Ma age from the Rb/Sr method (Augay, 1979).

3. Granite petrography and microstructures

3.1. The granitic facies

Two main granitic facies are recognized in the Millevaches massif:

– The porphyritic biotite granites, which outcrop mainly towards the centre of the northern half of the Millevaches massif (Fig. 1a and b). These contain large K-feldspar crystals, up to 4 cm in length, set in medium- to coarse-grained groundmass of plagioclase (oligoclase–andesine), K-feldspar, biotite and quartz. Parallel alignment of K-feldspar megacrysts and biotite is often observed and defines a magmatic lineation oriented N–S in the Pradines fault and NW–SE east of it (Mezure, 1980 and Stussi and Cuney, 1990).

– The two-mica leucogranites, which show a range in grainsize and texture, with average grainsize ranging from 1 mm in the fine saccharoidal varieties to 4–5 mm in the coarse varieties. They are composed of K-feldspar, plagioclase (albite–oligoclase), quartz, biotite and muscovite. A foliation and lineation are sometimes seen.

The cordierite–garnet leucogranites are formed by K-feldspar, plagioclase (oligoclase), quartz, cordierite, garnet and rare biotite. They represent the partial melting of granulite and have a defined foliation. They were the subject of only two measurements.

3.2. Microstructural observations

To determine the magma rheology during the magnetic fabric acquisition, a textural investigation has been made on 31 thin sections of representative samples. The samples have been subdivided into two types according to the magnetic lineation orientation.

Type I characterizes porphyritic biotite granite (MV77-MV78-MV15-MV84-MV35; Fig. 7) and two-mica leucogranites (MV7, MV9, MV10, MV12, MV6, MV16, MV50, MV44; Fig. 7) having a N–S magnetic lineation. Their textures show euhedral quartz crystals without substructure (Fig. 3a). Micas are not deformed. Many myrmekites, interpreted according to Hibbard (1987) as the result of crystallization of hydrous magma are located adjacent to the K-feldspars (Fig. 3b). These samples have preserved their primary magmatic textures.

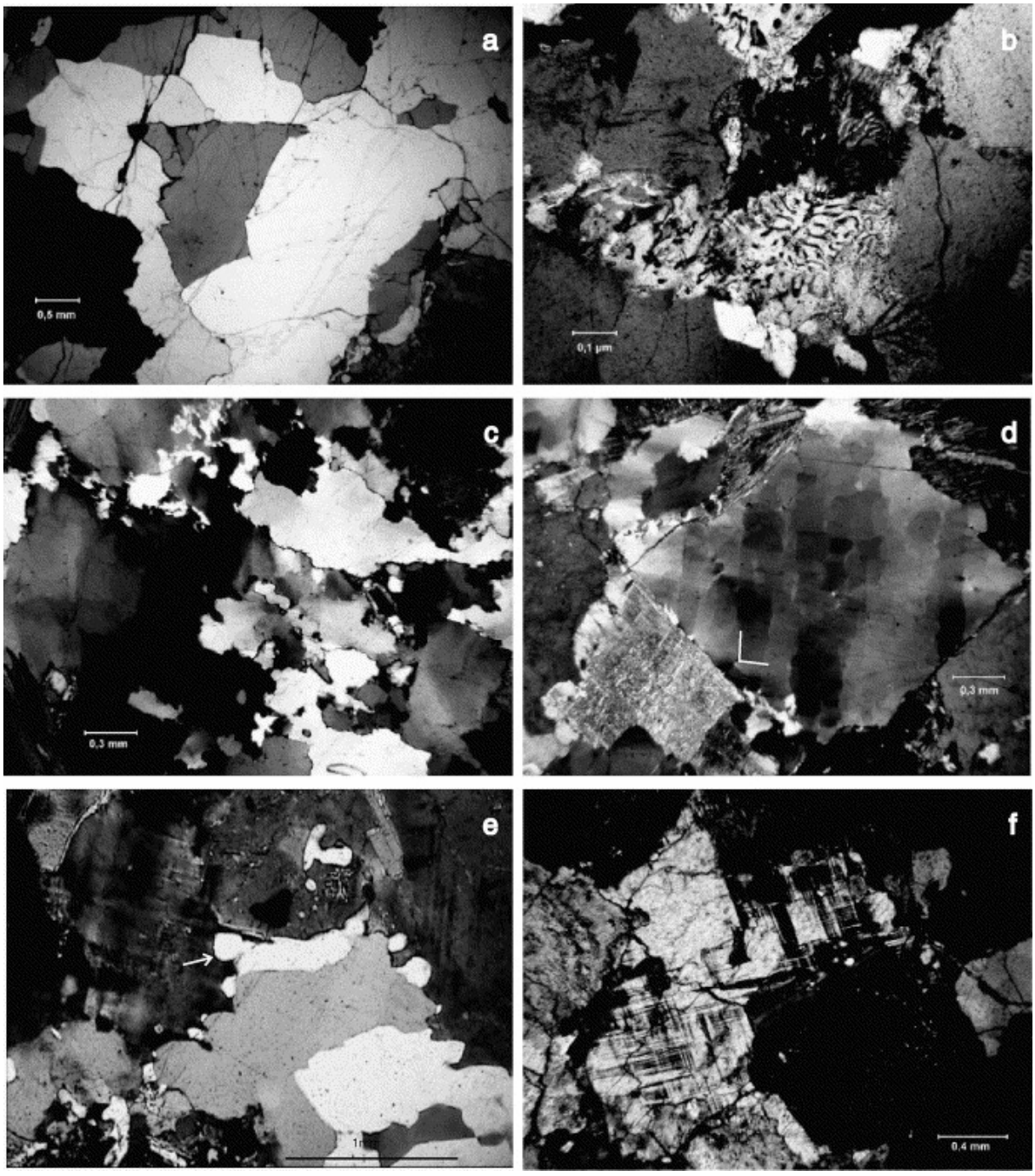

Fig. 3. Details of microstructures. Sections are cut perpendicular to foliation and parallel to lineation. (a) Large quartz crystals indicate primary formation. (b) Development of myrmekites adjacent to the K-feldspar. (c) Polycrystalline quartz aggregate showing an intense phenomenon of grain boundary migration typical of high temperature deformation. (d) Quartz with chess-board pattern indicating both $\langle a \rangle$ and [c] dislocation slip activity during high-temperature deformation. (e) Grain boundary cups between quartz and feldspar indicative of a type of solid-state diffusional creep deformed at elevated temperatures. Note the curved geometry of the quartz-feldspar phase boundary (underlined by the white arrows). (f) Orthoclase inversion to microcline typical of solid-state deformation.

Type II are porphyritic biotite granite (MV13, MV95, MV105, MV67, MV94, MV18, MV33; Fig. 7) and two-mica leucogranites (MV1, MV3, MV19, MV21, MV25, MV28, MV38, MV45, MV52, MV54, MV56; Fig. 7), most of them record a NW–SE magnetic lineation. Irregular grain shapes, bowed grain boundaries (Fig. 3c) are often observed, which are characteristic of a high mobility of the grain boundary at high temperature (Jessel, 1987). Quartz grains present frequently a chessboard-like texture (Fig. 3d), indicating both $\langle a \rangle$ and $\langle c \rangle$ dislocation slip occurred during high temperature (>600 °C) deformation under hydrous conditions (Mainprice and Bouchez, 1986 and Blumenfeld et al., 1986). The formation of cuspate grain boundary microstructures between quartz and feldspar are almost systematic (Fig. 3e) and are due according to Gower and Simpson (1992) to feldspar dissolution–precipitation at quartz–feldspar boundaries when oriented parallel to the foliation. This process of solid-state creep by diffusion occurs at high temperature (650–750 °C). The observed orthoclase inversion to microcline (Fig. 3f) is typical of solid-state deformation (Eggleton and Buseck, 1980). Most K-feldspars are affected by myrmekites. Some of the biotite grains show kinking or undulatory extinction microstructures, which suggest plastic deformation. Sample MV13 shows rectangular contouring of quartz grain boundaries illustrating high mobility of grain boundaries at elevated temperature (Gapais and Barbarin, 1986).

4. Magnetic fabrics of the Millevaches granites

4.1. Sampling and magnetic mineralogy

We collected about 700 oriented cores from 105 regularly spaced sites in the north-central part and in the south-central part of the Millevaches (Fig. 7). In combination with Jover's (1986) study in the northern part of the massif, a good sampling coverage has been achieved. Sampling at each site was performed with a portable gasoline drill. Five to ten cores of 7 cm in length and 2.5 cm in diameter well distributed on the outcrop were extracted. When possible, both magnetic and solar compasses were used to measure core orientations. The difference between them was negligible (<5°). The samples are mainly composed of porphyritic biotite granites and biotite–muscovite leucogranites. A few (two samples) garnet–cordierite leucogranites were also collected.

To identify the minerals carrying the magnetic signal, we measured hysteresis loops for several representative specimens. For this, we used a translation inductometer within an electromagnet providing a field of up to 1.0 T at the Paleomagnetic Laboratory of Saint Maur (Paris). We observed during increasing and decreasing magnetic fields the linear superimposition of the two curves (Fig. 4). Therefore, the anisotropy of magnetic susceptibility (AMS) measurements can be confidently related to the mica (mainly biotite and muscovite) subfabric (Fig. 4).

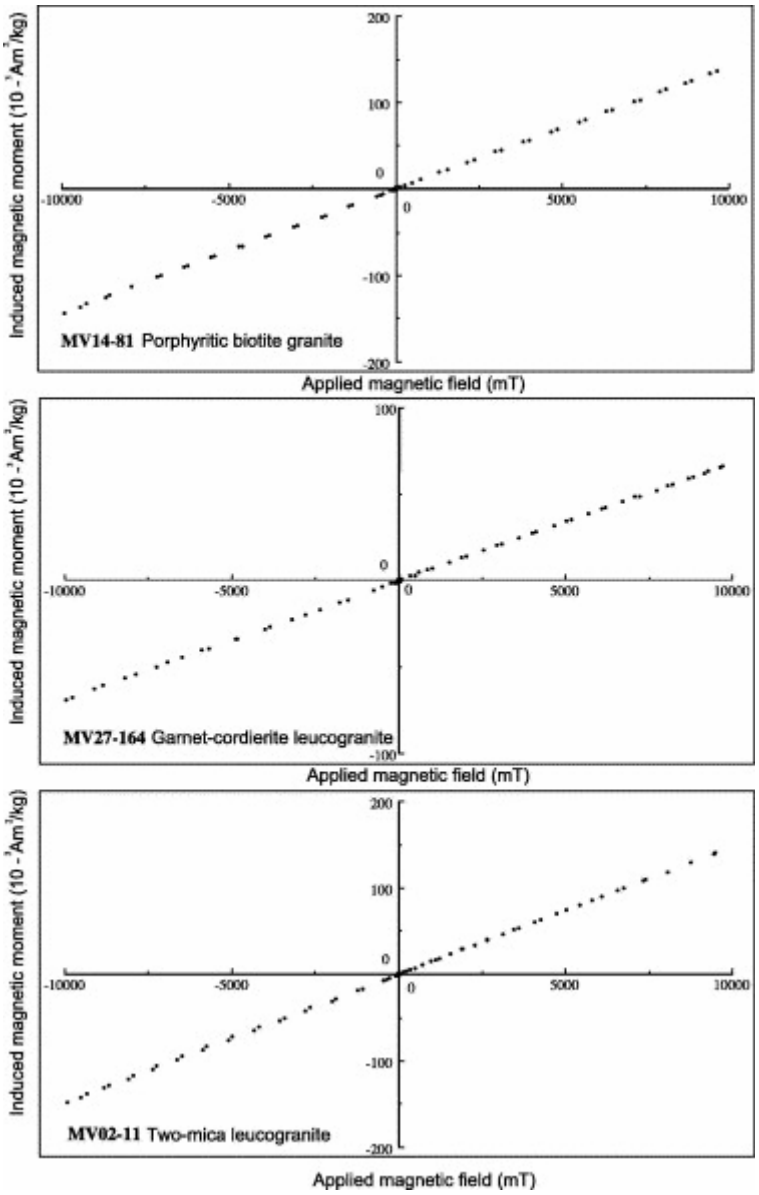

Fig. 4. Hysteresis curve showing linear and superposing induced magnetic moments with respect to increasing and decreasing applied magnetic fields.

Bulk magnetic susceptibility (K) was measured with a KLY3 kappabridge. The K values of two-mica leucogranites were weaker than those of the porphyritic biotite granites (Fig. 5). The K histogram shows a unimodal asymmetric distribution, ranging from 10 to 180×10^{-6} SI and with a mean value of 60×10^{-6} SI (Fig. 5). The low values are consistent with the absence of high susceptibility ferro- or ferri-magnetic minerals in our samples.

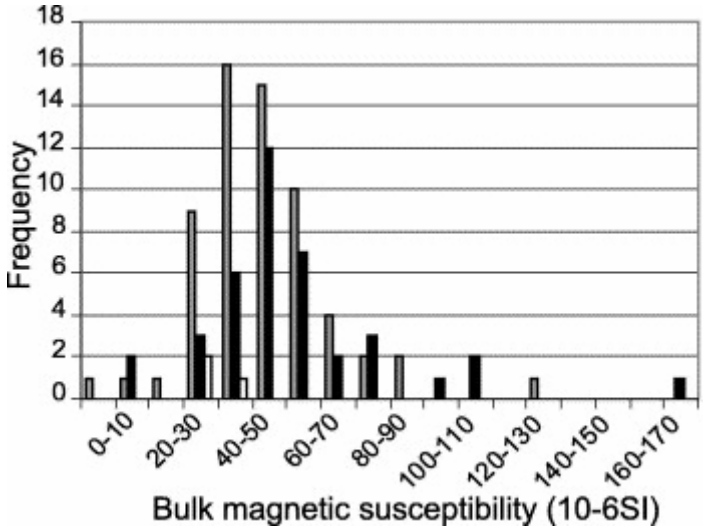

Fig. 5. Frequency histogram for bulk magnetic susceptibility. Grey: two-mica leucogranites; black: porphyritic biotite granites; white: garnet–cordierite leucogranites.

4.2. Degree of anisotropy (*P′*) and shape parameter (*T*)

To describe the shape of the AMS ellipsoid and the degree of anisotropy, two parameters, T and P' (Jelinek, 1978, Jelinek, 1981 and Hrouda, 1982) are computed for each site (see Table 1). Both two-mica leucogranites and porphyritic granites show common magnetic fabric characteristics (Fig. 6). The plot of the shape (T) and degree of anisotropy (P') parameters show a mixture of linear (prolate) and planar (oblate) shapes between these two principal types of granites (Fig. 6). However, the spatial distribution of the two parameters is more complex. The oblate shape has been characterised along the St Michel de Veisse fault ($T>0.35$) and between Eymoutiers and Peyrelevade ($0<T<0.35$) (Jover, 1986). On the other hand, the prolate type ellipsoid has been well defined along the Pradines fault ($T<-0.35$) and to the east ($-0.35<T<0$). The prolate-dominated shape parameter has been also observed in the north of Eymoutiers district with T value varying between −0.35 and 0. More than 90% of sites show a relatively weak degree of anisotropy with P values less than 8%. Some anomalous sites (less than 10% of the total population), mainly distributed in the northern part of the massif along the St Michel de Veisse fault indicate the possible influence of tectonic motion of this fault. For the AMS, it is worth noting that the Pradines fault is characterised by low P' values ($P<10\%$). The generally low P' values suggest that the investigated AMS in this study was acquired during the emplacement of granitic massifs (Hargraves et al., 1991).

Table 1. : Anisotropy of magnetic susceptibility data. *N*: number of specimens; *K*: bulk magnetic susceptibility in 10^{-6} SI; Dec, Inc, α_{95min}, α_{95max}: declination, inclination, Bingham (1964) bimodal statistics data, respectively, in degrees; *P′*: anisotropy degree; *T*: shape parameter (Jelinek, 1981 and Hrouda, 1982)

Site	**Type**	***N***	***K***	**K1**				**K3**				***P′* (%)**	***T***
				Dec	**Inc**	**α_{95min}**	**α_{95max}**	**Dec**	**Inc**	**α_{95min}**	**α_{95max}**		
MV1	2 micas γ	5	30.7	186.1	44.9	4.3	6.5	53.7	34.5	0.6	26.4	4.7	−0.138
MV2	2 micas γ	6	51.7	71.7	33.9	8.3	22.1	220.6	49.1	2.5	10	4.3	−0.274
MV3	2 micas γ	6	60.2	49.5	41.3	9.1	32.5	190.1	43.2	10.4	12.8	2.6	0.83
MV4	2 micas γ	8	51.6	114.9	14.3	6.1	11	214.9	33.9	4.1	7.7	4.9	0.389
MV5	2 micas γ	7	34.7	116.4	27.5	2.7	11.4	23.9	3.4	5.3	8.8	4.3	−0.047
MV6	2 micas γ	7	37.7	138.8	24.8	5.8	10.6	339	62.9	4.1	6.4	5.4	0.71
MV7	2 micas γ	9	43.5	8.3	42.7	6.6	10.5	176.7	48.2	8.4	23.7	3.7	0.455
MV8	2 micas γ	8	37.5	231.4	16.8	4.5	17.8	0.5	63.1	3.9	4.9	3.9	0.698
MV9	2 micas γ	8	56.2	345.9	15.3	3.6	4.8	255.1	4.7	2.1	9.8	9.7	0.183
MV10	Porphyritic Btγ	6	60.8	206.6	5.6	4.1	25.5	296.6	70.6	3	15	7.3	0.63
MV11	Porphyritic Btγ	5	55.7	11.7	23.3	1.9	5.9	189.4	66.7	2	6.2	8.9	0.364
MV12	2 micas γ	6	44.9	27.7	7.4	5.1	28.1	284	65.6	4.1	5.5	5.9	0.815
MV13	Porphyritic Btγ	4	51.2	178.1	10.3	4.4	17	57	72.5	5.2	13.2	4.4	0.159
MV14	Porphyritic Btγ	4	63.1	152.4	10.4	11.4	29.5	252.4	38.9	6.9	20	3.7	0.111
MV15	2 micas γ	5	71.2	20.5	63.5	10.4	14.1	163.9	20.6	7.9	20.1	3.5	−0.122
MV16	2 micas γ	8	55.9	345.8	11.7	3.5	8.6	206.5	75.4	1.8	5.2	12.2	0.679
MV17	Porphyritic Btγ	4	47.2	125.4	37.2	11.3	25.2	31.3	5.6	10.2	11.8	4.8	0.053
MV18	Porphyritic Btγ	6	66.7	139.5	0.6	5.7	9.5	50.5	79.1	6.5	21.8	7.4	−0.047
MV19	2 micas γ	10	61.4	137.2	22.5	7.6	13.3	3	59.3	7.2	13.4	8.4	0.394
MV20	2 micas γ	7	47.9	325.2	21.7	14	31.6	172.1	73.6	13.1	14.9	5.5	0.735
MV21	2 micas γ	6	51.2	300.7	19.1	5.9	19.1	188.8	44.1	4.4	8.5	12.1	0.736
MV22a	2 micas γ	6	69.9	87.8	9	4	5.1	317.9	75.9	3.4	8.5	8.6	0.11
MV22b	2 micas γ	3	69.9	113.3	18.6	0.1	22.5	236.1	54.8	2.8	22.5	8.6	0.11
MV23	2 micas γ	5	52.5	229.2	46.3	9	14.8	110.9	23.8	6	21.3	5.4	0.339
MV24	2 micas γ	7	43.7	179.3	27.7	17.7	27.2	80.4	29.3	13.7	19.2	2.3	0.34
MV25	2 micas γ	9	46.1	111.2	38.7	3.7	6.6	239.7	38.3	3.8	15.2	3.8	−0.332
MV26	2 micas γ	9	39.3	86.7	27.5	3.4	6.3	265.5	61.7	6.1	23.9	4.8	−0.622
MV27	Grt–Crd leucoγ	9	39.6	179	51.8	11.8	18.6	62.5	22.5	6.6	17.1	2.4	0.773
MV28	2 micas γ	7	41.9	120.1	12.7	3.9	12.9	227.8	56.3	10.7	39.5	15.8	0.63
MV29	2 micas γ	7	47.8	120.1	12.7	3.9	12.9	227.8	56.3	10.7	39.5	4.9	−0.714
MV30	2 micas γ	4	57.6	310.7	4.8	16.7	26.8	214.1	53.1	8.5	18.4	5.3	0.811

Site	Type	*N*	*K*	K1				K3				*P′* (%)	*T*
				Dec	Inc	α_{95min}	α_{95max}	Dec	Inc	α_{95min}	α_{95max}		
MV31	Porphyritic Btγ	7	49	0.6	8.9	4.3	8.4	192.1	80.2	7.2	20	4.6	−0.292
MV32	Porphyritic Btγ	5	56.3	214.1	10	15.2	44.3	113.4	65	19.3	26.3	15.6	0.583
MV33	Porphyritic Btγ	7	67.4	138.9	2	2.8	10.2	229.2	53.6	8.9	21.5	5.2	−0.243
MV34	Porphyritic Btγ	5	32.4	5.9	5.6	14.7	23.2	271.1	34.9	19.4	26.5	4.7	−0.219
MV35	Porphyritic Btγ	8	60.1	357.1	8	15	23.5	89.5	10.8	7.5	20.1	3.8	0.331
MV36	2 micas γ	6	92.6	337.4	8.1	13.3	27.6	229.4	44.4	14.6	19.7	4.2	0.586
MV37	Porphyritic Btγ	7	86.2	173.7	20.9	11.2	27.7	71.8	42.1	8.6	23.8	4.2	0.147
MV38	2 micas γ	8	49.5	165.5	10.7	9.1	21.2	277.3	43.4	14.3	18.2	7.8	0.439
MV39	2 micas γ	6	58.3	25.8	13.6	7.8	13.7	121.7	21.3	7.1	24.3	5.8	−0.141
MV40	Grt–Crd leucoγ	9	47.3	3.1	21.4	8.1	11.3	254.9	41.1	9	35.7	5.5	−0.626
MV41	Porphyritic Btγ	5	67.4	19.7	58.7	9.2	27.3	238.9	22.7	3.7	15.6	6.2	0.544
MV43	Porphyritic Btγ	6	172.9	241.5	9.9	9.1	37.4	133.4	30.5	3.5	16	3.2	0.706
MV44	2 micas γ	7	97.3	151.1	16.8	11.1	22.5	246.5	3.7	9.9	20	4.1	−0.006
MV45	2 micas γ	7	73.3	252.7	22.8	3.2	15.3	69.8	66.9	3.8	11.7	4.3	0.263
MV47	2 micas γ	6	51.5	319.3	11.2	11.6	28.5	216.7	42.8	3.9	12.9	2.5	0.394
MV48	2 micas γ	6	59.6	87.4	62.7	3.7	38.5	341.9	7.5	3.4	6.7	6.9	0.827
MV49	2 micas γ	6	83.9	46.1	31.1	13.1	34.8	304.3	5.6	12.4	19.1	6.3	0.671
MV50	2 micas γ	6	134.2	1.8	20.5	4	12.6	266.4	13.2	6.8	13.3	3.1	−0.153
MV51	2 micas γ	7	66.4	327.4	24.2	6.1	9.4	228.8	20	4.2	14.4	4.9	0.142
MV52	2 micas γ	9	57.6	130.3	17.9	3.9	13.4	337.4	70.8	3.9	8.9	3.4	0.136
MV53	2 micas γ	6	43.5	359.5	25.4	7.3	30.9	240.8	32.9	6	21.9	2.7	0.107
MV54	2 micas γ	6	14.8	119.2	31.6	10.7	27	272.4	61.2	13.2	22	9.4	0.035
MV55	2 micas γ	6	58	140.3	10.7	2.3	5.6	258	68.5	4.9	11.6	4.8	−0.247
MV56	2 micas γ	6	116.5	128.5	2.9	5.6	12.3	227.3	48.4	4.3	28.8	5.1	−0.39
MV57	Porphyritic Btγ	6	58.5	137.7	31.7	5.4	6	237.4	12.9	4.8	15.9	6.1	−0.379
MV58	Porphyritic Btγ	6	57.5	161.1	29.3	3.5	5.4	17.7	54.7	4.4	19.2	4.5	−0.547
MV59	2 micas γ	6	36.4	111.9	47.6	7	22.5	352.6	25.7	5.7	7.7	6.8	0.323
MV60	Porphyritic Btγ	6	39.4	121.5	4.5	1.3	6.9	22.7	61.3	5.8	17.8	6	0.094
MV61	2 micas γ	7	37.8	301	0.5	9.7	20	28.9	51.1	9.2	31.4	3	−0.31
MV62	2 micas γ	6	49.4	154.2	3.7	3.9	8.7	348.5	84.6	3.7	13.4	5.2	−0.305
MV63	2 micas γ	5	47.2	311.9	8.6	3.8	15.7	45	23.5	7.1	25.5	5.6	−0.148
MV64	2 micas γ	8	43.8	108.6	1.4	3.8	14.5	6.1	72.7	3.3	12.9	7.7	0.508
MV65	2 micas γ	8	56.6	331.3	7.9	3	11.9	65.2	34.3	8.3	25.2	4.3	−0.278

Site	Type	*N*	*K*	K1				K3				*P′* (%)	*T*
				Dec	Inc	α_{95min}	α_{95max}	Dec	Inc	α_{95min}	α_{95max}		
MV66	2 micas γ	8	48.2	322.1	9.6	5	6.5	62.5	43.3	5.1	17.5	5.3	−0.295
MV67	Porphyritic Btγ	6	50.5	312.6	3.8	8.4	17.8	222.2	54.2	11	25.5	3.3	−0.387
MV68	Porphyritic Btγ	6	57.2	128.8	7.6	5.4	13.3	233.4	40.2	3.9	32.2	3.7	−0.699
MV69	Porphyritic Btγ	7	40.4	111.8	1.6	9	29.6	141.7	89.6	6.9	19.2	4.6	0.48
MV70	Porphyritic Btγ	7	54.1	139.9	4.3	3	5.3	262.5	82.1	3.1	11	9.8	0.102
MV71	Porphyritic Btγ	5	50.6	144.6	6.7	4	7.2	40	64.3	2.4	5.8	7.3	0.006
MV72	Porphyritic Btγ	6	81.7	330.7	6.3	9.8	13.6	221.9	71.1	9.8	14	7.5	0.314
MV73	Porphyritic Btγ	8	56.5	164.6	9.8	3.6	16.3	272.2	71.2	6.5	15.1	4.9	0.185
MV74	Porphyritic Btγ	6	79	330.4	15.8	9.5	18.2	201.4	67.4	3.6	20.5	4.6	−0.005
MV75	Porphyritic Btγ	4	46.6	342.7	31.8	12.7	18.2	239.1	26.4	11.5	23.3	3.2	−0.146
MV76	Porphyritic Btγ	6	42.4	328.8	19.5	2.2	17.8	230.9	23.9	10.6	16.2	3.6	−0.044
MV77	Porphyritic Btγ	7	68.4	352.1	15.6	5.7	14.5	254.5	9.6	9.2	24.8	4.3	−0.558
MV78	Porphyritic Btγ	8	58.2	167.2	1.5	5.1	12.8	71.4	76.3	4.8	15.5	6.9	−0.258
MV79	2 micas γ	8	44.3	214.4	4.6	4.5	29.4	319.2	71.1	3.7	5.6	4.4	0.788
MV80	2 micas γ	6	61.5	171	21.2	3.8	8.1	24.8	64.4	5.1	7.4	7.4	0.374
MV81	2 micas γ	7	58.8	337.2	18.3	2	10.9	106	59.8	3.2	14.6	5.4	0.049
MV82	2 micas γ	6	65.1	313.7	22.6	6	15.8	202.7	41.7	3.5	8.2	6	0.749
MV83	2 micas γ	4	9.7	9.6	10.8	3.1	36.5	198.7	77.6	3.6	8.6	3.6	0.547
MV84	Porphyritic Btγ	6	80.9	345.5	20.7	3.6	17.5	247.6	16.9	4.1	13	6.1	0.238
MV85	Porphyritic Btγ	6	16.5	327.6	22.8	15.4	19.4	216.3	59.5	8.3	43.4	20	−0.351
MV86	Grt–Crd leucoγ	6	35.2	339.2	4.7	7.7	14.3	244.4	56.1	9.3	14.6	13.1	0.26
MV87	Porphyritic Btγ	6	47.6	328.8	8.6	4.3	13.5	226.6	50	3.9	4.5	7.3	0.455
MV88	2 micas γ	7	83.1	312.4	21.3	8.6	15.6	207.9	6.9	5.5	36	5.2	−0.718
MV89	2 micas γ	8	72.1	47.1	44.5	14.8	26.7	229.4	42	7	30.8	2.3	−0.61
MV90	2 micas γ	7	49.6	167	31.4	5.5	16.2	259.8	21.5	10.8	40.6	4.3	−0.768
MV91	2 micas γ	6	34.2	101.9	36.6	16	28.1	4	4.6	27.1	36.4	3	−0.617
MV92	2 micas γ	9	52.4	95.2	25	4.3	5.9	319.8	56.9	4.5	5.9	5.5	0.379
MV93	2 micas γ	7	27.6	232.6	19.8	9.3	23.3	140.2	1.1	8.7	14.9	2.1	0.576
MV94	Porphyritic Btγ	5	54.8	359.8	6.1	13.1	30.1	131.8	80.8	1.4	19.9	2	0.359
MV95	Porphyritic Btγ	9	31.5	130.6	2.1	8.5	15.2	40.4	77.7	13.8	20.2	6.1	−0.1
MV96	Porphyritic Btγ	6	73.1	54	39.1	21.7	30.8	233.1	57.1	9.9	27.5	3.3	0.36
MV97	Porphyritic Btγ	7	13.8	184.7	8.2	9.2	13.2	279.6	33.4	12.1	20.9	6.5	−0.181
MV98	Porphyritic Btγ	7	103.8	162.8	3.9	4.1	8.6	32	80.9	2.1	21.8	4.1	−0.224

Site	Type	*N*	*K*	K1				K3				*P′* (%)	*T*
				Dec	Inc	α_{95min}	α_{95max}	Dec	Inc	α_{95min}	α_{95max}		
MV99	2 micas γ	7	69.7	323	38.4	11.8	23.8	198.5	38.8	12.5	29	4.2	−0.343
MV100	2 micas γ	8	73.5	341.9	8.2	8.9	15.5	108.6	80.2	10.3	16.7	4.8	0.023
MV101	2 micas γ	8	60.1	126.9	12.6	9.6	17.5	217.2	43.4	15.4	32.5	3	−0.52
MV102	2 micas γ	6	65.7	229.4	19.3	4.2	5.9	130.5	24.3	3.4	5	2.3	0.269
MV103	2 micas γ	6	47.5	352	61.4	18.9	37.1	157.1	23.7	5.8	39.7	4.8	−0.023
MV104	2 micas γ	8	39.7	139.6	4.1	5.3	18.8	50.2	74.2	9.1	20.3	5.3	0.137
MV105	Porphyritic Btγ	8	111.2	283	1	4	11.9	191.3	66	4.2	6	9.4	0.552

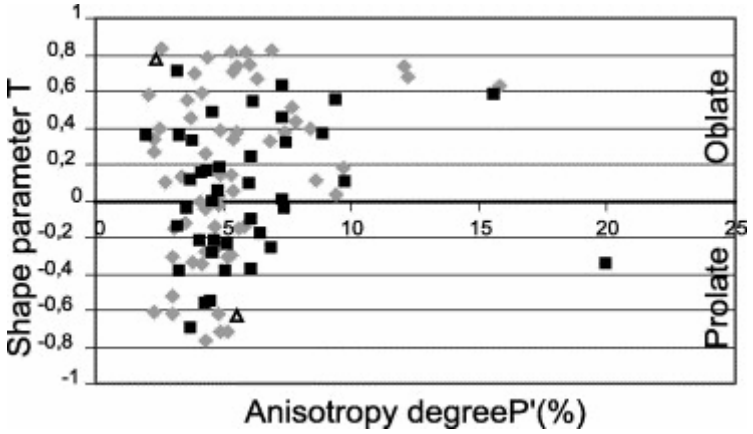

Fig. 6. Plots of the shape (*T*) and anisotropy degree (*P′* %) parameters showing a homogeneous repartition between the linear (prolate) and planar (oblate) shapes. Grey diamonds: two-mica leucogranites; black squares: porphyritic biotite granites; white triangles: garnet–cordierite leucogranites.

4.3. Magnetic fabric pattern

The AMS measurements were carried out using a KLY3 kappabridge spinner. The principal axes of the magnetic susceptibility ellipsoid, K_{max}, K_{int} and K_{min}, were determined from each specimen and an average orientation of each axis was calculated for each site with Bingham (1964) bimodal statistics (see Table 1 for the results). Thus for each site, the site-average orientation and confidence intervals at the 95% level, corresponding to the α_{95min} and α_{95max} were computed (Table 1). If confidence level of a magnetic axis, K_{max} and/ or K_{min} axes, is smaller than 20° within a site, the magnetic axis is considered to be well-defined, if not the site-average orientation is considered unreliable. In terms of petrofabrics, K_{max} and K_{min} refer, respectively, to the magnetic lineation and the pole of the magnetic foliation. Their orientations are used to define the magnetic fabric pattern of the Millevaches granite and for the interpretation of the flow structure of the granitic plutons.

Fig. 7 presents equal-area stereographic projections of three principal axes of magnetic susceptibility for each site in the centre and southern part of the Millevaches massif. Specimen results, average orientations, and confidence ellipses are plotted. Fifty-two percent

of the sample population shows well-grouped orientations with three well-defined principal axes (samples indicated by the black square on each stereogram in Fig. 7 and Table 1). Twenty-two percent illustrate a well-grouped K_{max} axes with scattered distribution of K_{int} and K_{min} (samples in black circle in Fig. 7 and Table 1). Twenty-six percent produced well grouped K_{min} with a scattered distribution of K_{max} and K_{int} (samples underlined Fig. 7 and Table 1). Fig. 8 and Fig. 9 represent, respectively, the Millevaches magnetic lineations and foliations map (AMS data from our study area plus AMS data from Jover (1986)).

At the scale of our study area, the fabric pattern of the Millevaches massif reveals sub-horizontal lineations (Fig. 7 and Fig. 8) for both the two-mica leucogranites and the porphyritic biotite granites, with a predominantly NW–SE orientation. In the southern part of the study area (S.P. on Fig. 7 and Fig. 8), the majority of magnetic lineations have a NW–SE orientation with a shallow plunge that rarely exceeds 30°. The magnetic foliations strike NW–SE with a dip ranging between 0 and 40° (Fig. 7 and Fig. 9). In the west centre part (W.C.P. on Fig. 7 and Fig. 8), the magnetic lineations are sub horizontal and trend N–S. Some NE–SW magnetic lineations are observed (MV43, MV49, MV10, MV12, MV79; Fig. 7). The magnetic foliations located in the inner part of the Pradines fault present dip varying between 90 and 45° (Fig. 7 and Fig. 9). The others going eastward, become sub horizontal (MV31, MV32, MV13, MV79, MV80, MV81, MV83, MV10, MV11, MV12, MV85, MV86; Fig. 7). In the east centre part (E.C.P. on Fig. 7 and Fig. 8), the NW–SE magnetic lineations are still dominant, but N–S and NE–SW directions are also measured. The NE–SW lineation is restricted to a few sites of two-mica leucogranites (e.g. sites MV3—MV8; Fig. 7). The magnetic foliations are more scattered. Most of the sites have a low dip except where they become parallel to the Ambrugeat and Felletin faults (MV23, MV24, MV1, MV90; Fig. 7). Towards the Argentat fault the magnetic foliation dip decreases gradually and the magnetic lineation strikes E–W with a sub-horizontal dip (MV45; Fig. 7), which is in good agreement with the Jover data just northward of the MV45 site.

The NE–SW lineations, perpendicular to the more general trends, cannot be taken into account for several reasons: these sites present (i) relatively low magnetic susceptibility intensity (37.5, 44.9 and 44.3×10^{-6} SI for MV 8, MV 12 and MV 79, respectively; Table 1); (ii) poor statistical precision parameter for AMS data with wide confidence radii at the 95% level (e.g. 32.5, 25.5, 28.1, 37.4, 34.8 and 29.4° for MV3, MV10, MV12, MV43, MV49 and MV79, respectively; Table 1); (iii) they are characterized by oblate ellipsoid.

According to Jover (1986) who carried out measurements north of Royère-de-Vassivière (Fig. 8 and Fig. 9), the N–S sub-horizontal magnetic lineations are associated with vertical magnetic foliation within the porphyritic biotite granite. Between Royère-de-Vassivière and Eymoutiers, our measurements of the two-mica leucogranites show the same observations (Fig. 7, Fig. 8 and Fig. 9). This is in agreement with the presence of the Pradines wrench fault, which sometimes does not show mylonitic structures. This author mentioned occurrence of the NW–SE sub-horizontal lineations mainly in the two-mica leucogranites. However, our study confirms in the east and central parts the porphyritic biotite granites also recorded the NW–SE lineations (Fig. 9). Magnetic foliations with steeper dip are often measured parallel to the St Michel de Veisse fault (Fig. 9). Within the northeastern part of the massif, foliation planes follow the edge shape of the pluton and strike E–W to NW–SE parallel to St Michel de Veisse fault to become southward, N–S, like the Felletin ductile fault (Fig. 9).

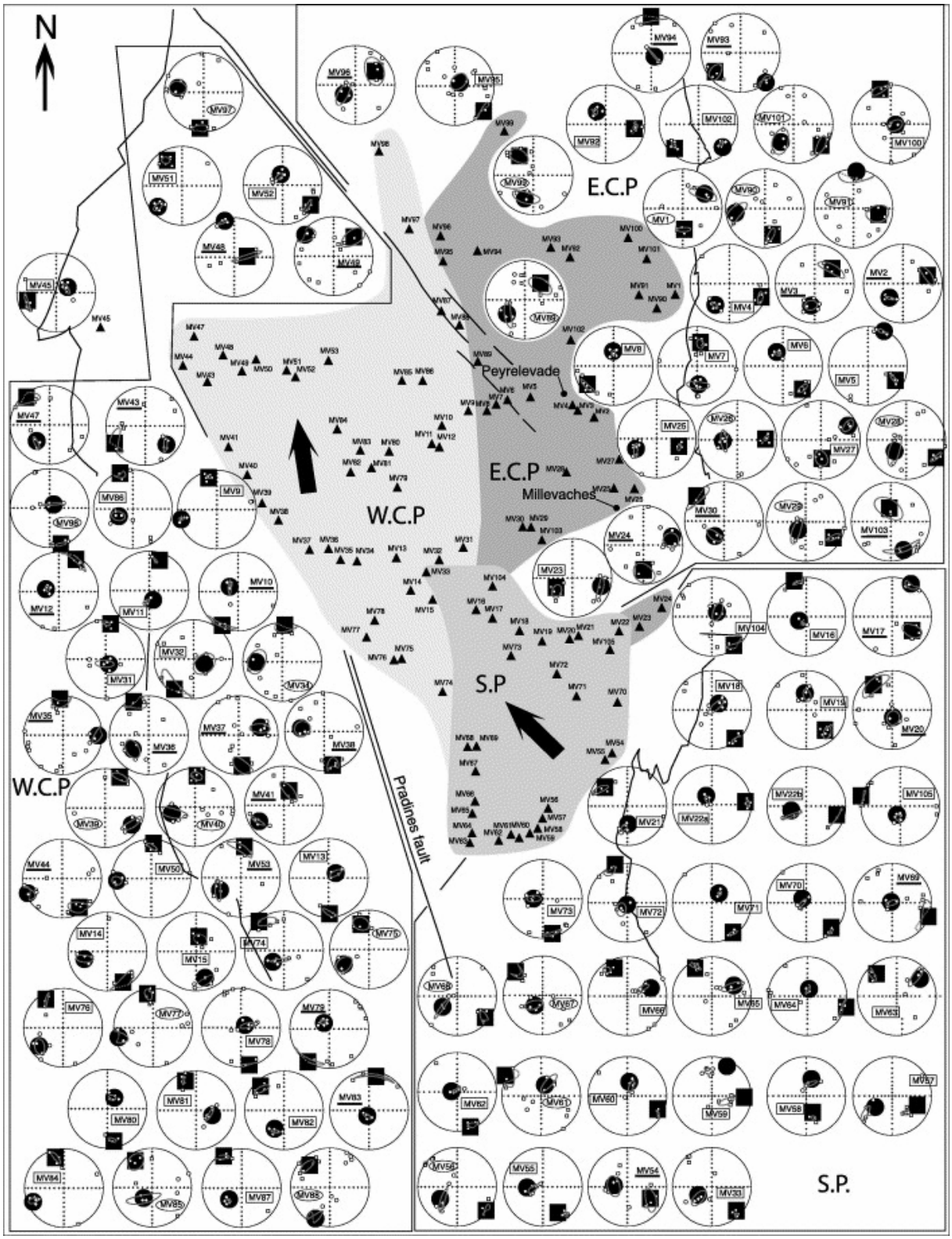

Fig. 7. Equal area-projection of AMS results for each sampling site (black triangles) of the Millevaches massif. S.P.: southern part; W.C.P.: west centre part; E.C.P.: east centre part; squares and circles are K1 (magnetic lineation) and K3 (pole of magnetic foliation), respectively. Small white dots and larger black ones represent, respectively, specimen and average orientation directions. Confidence ellipses are drawn around average orientation direction.

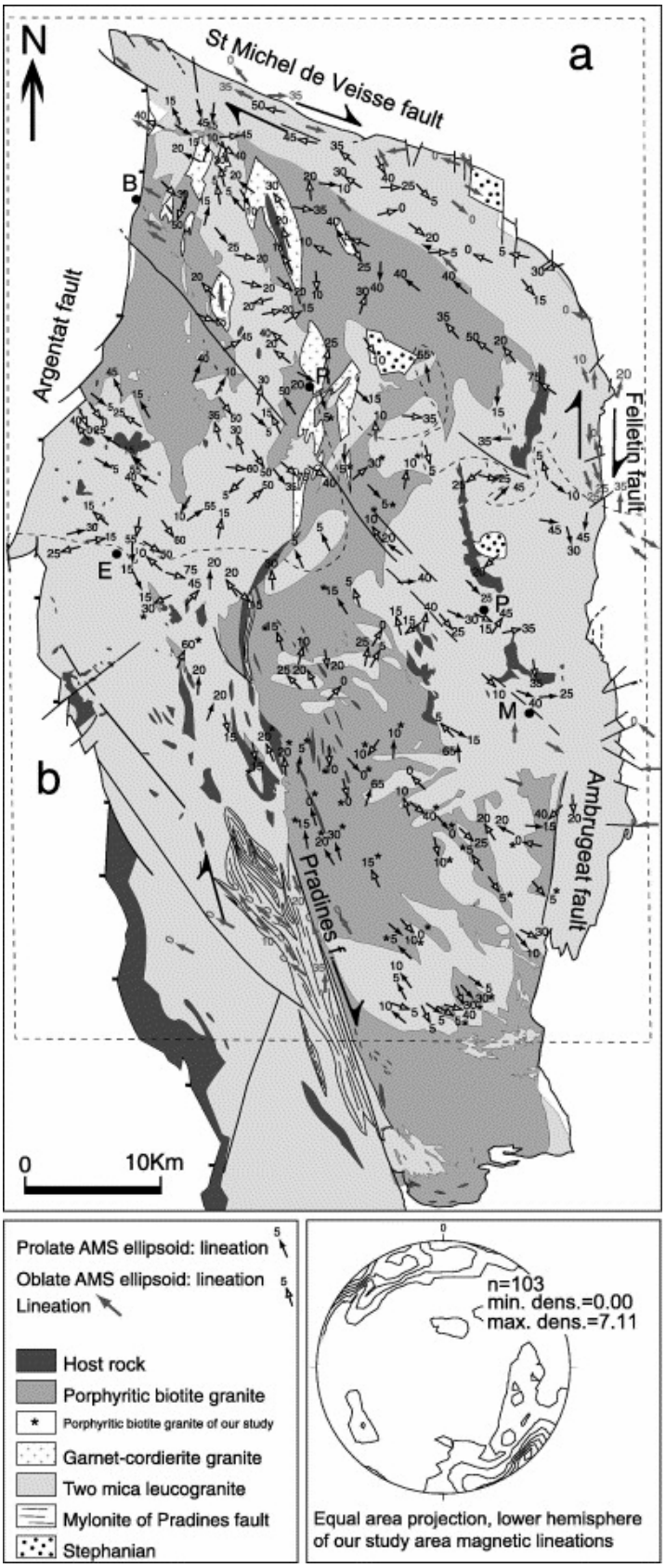

Fig. 8. Magnetic lineations of the Millevaches massif: (a) AMS data from Jover (1986), (b) AMS data from our study area. M: Millevaches; P: Peyrelevade; E: Eymoutiers; R: Royère-de-Vassivières; B: Bourganeuf.

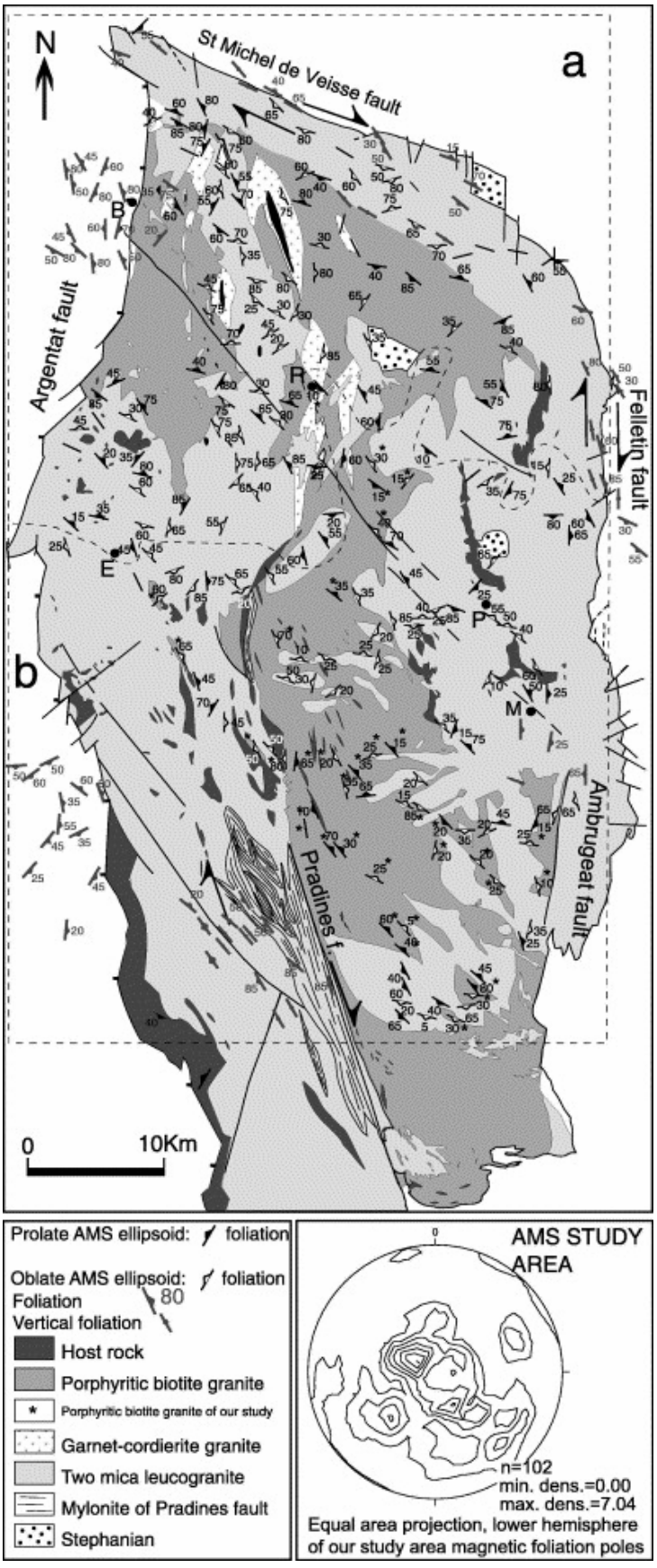

Fig. 9. Magnetic foliations of the Millevaches massif: (a) AMS data from Jover (1986), (b) AMS data from our study area. M: Millevaches; P: Peyrelevade; E: Eymoutiers; R: Royère-de-Vassivières; B; Bourganeuf.

5. Gravity study

Through the analysis and the inversion of the residual Bouguer anomaly, previous work (Gébelin et al., 2004) allowed us to model the Millevaches massif as a laccolith with a thickness of 2–4 km from north to south and from west to east with local rooting down to about 6 km depth in its eastern and southern extremities. To study in more detail the structure of the Millevaches massif at depth, four 2D gravity cross-sections oriented E–W across the massif are presented (profiles A, B, C and D; Fig. 10). In addition, two N–S regional gravity cross-sections are discussed (profiles E and F; Fig. 10); they suggest relationships of the Millevaches massif with the surrounding granites.

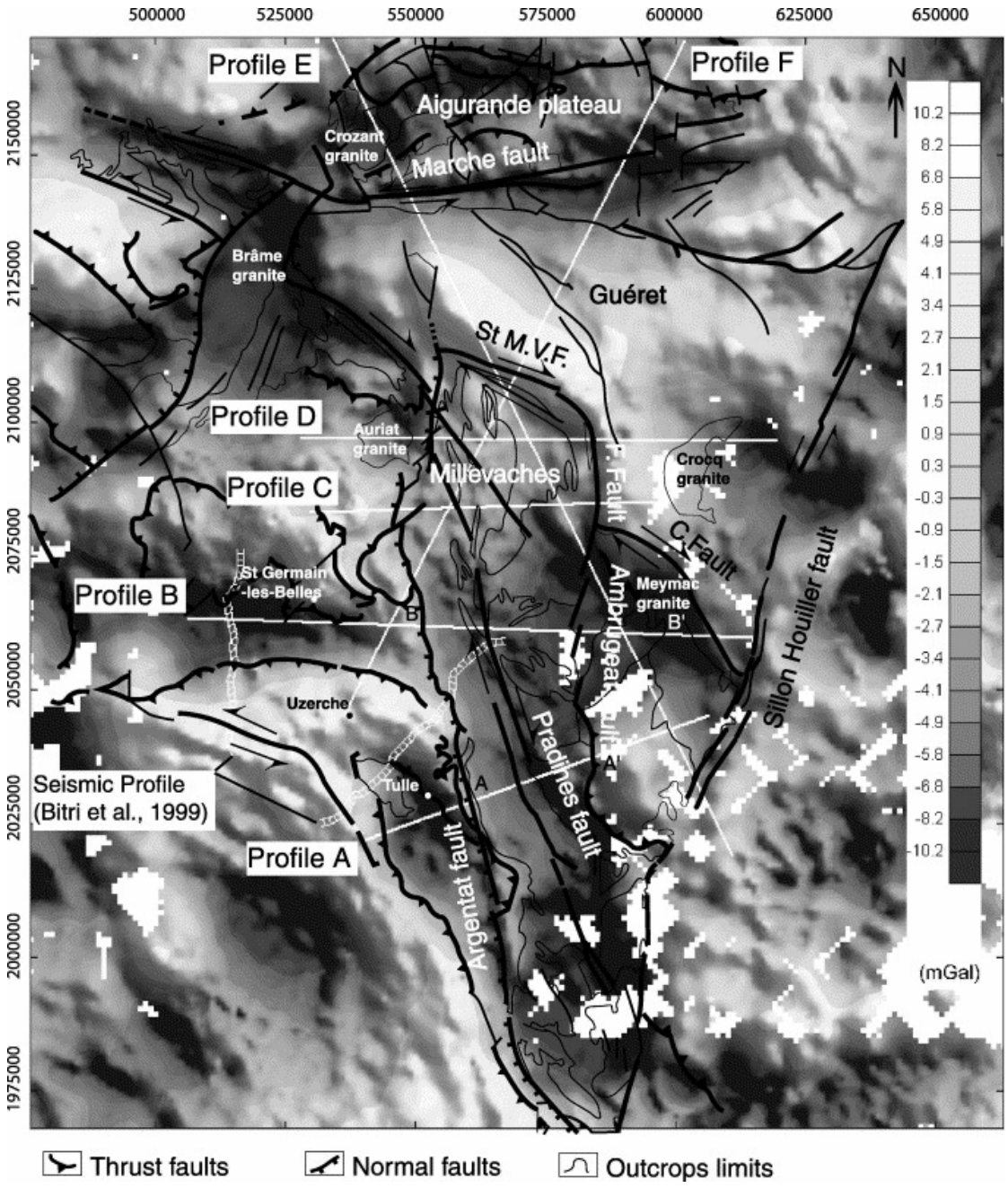

Fig. 10. Profile location on Residual Bouguer anomaly map of the north-western part of the Massif Central. White circle corresponds to the Bitri et al. (1999) seismic profiles location.

5.1. Constraints prior to modelling

To constrain the gravity models, all the available independent information has been taken into account. The outcropping limits of the surface formations were derived from the geological maps (Cuney and Stussi, 1989) and our field observations.

The densities of the different rock units were measured by Gébelin et al. (2004). The densities of the main units are: ρ=2640 kg/m^3 for the two-mica leucogranites, ρ=2620 kg/m^3 for the porphyritic biotite granites, ρ=2750 kg/m^3 for the micaschists, ρ=2780 kg/m^3 for Bt/Sil gneiss, ρ=2720 kg/m^3 for Crd anatectic of 'aubussonite' type. It must be kept in mind that due to the weak density contrast between porphyritic biotite granites and two-mica leucogranites, contacts at depth between these facies are poorly constrained. The deepest modelled interface is the bottom of the micaschists, which lies on an undifferentiated substratum of density 2800 kg/m^3, i.e. possible density contrasts deeper than the micaschists are not taken into account. This assumption is valid because we model the residual Bouguer anomaly: in this case, only short to intermediate wavelength anomalies are considered, which are mainly associated with sources shallower than approximately 10 km depth. In order to avoid edge effects, all profiles were extended by 100 km at both ends.

The Limousin substratum belongs to the para-autochthonous unit upon which internal and higher grade metamorphic units were thrusted (Ledru et al., 1989). We chose the same structure, which consists from top to bottom of Crd anatexites (UGU), with or without high-pressure rock, Bt/Sil gneiss (LGU) and micaschists.

In our modelling, structural relationships and depth of the deep para-autochthonous gneiss and micaschist formations is adapted from Argentat deep seismic profile (Bitri et al., 1999) that crosses the western border of the Millevaches plateau (Fig. 10). The seismic interpretation that we integrate in our gravity profile A shows that the Argentat normal fault offsets the bottom of the micaschists from about 14 km depth west of the Millevaches to about 7 km depth underneath the Millevaches massif. Deep para-autochthonous gneissic and migmatitic series, on both sides of the massif, have been revealed by the seismic profiles, but they are not recognized below the granite, which lies directly on the micaschists. As a hypothesis, this geometry of the deep metamorphic units has been generalized northwards along the western border of the Millevaches massif, and eastward because the E–W gravity anomaly is roughly symmetric on both sides of the Millevaches.

5.2. 2D gravity modelling (see location on Fig. 10)

Profile A (Fig. 11): The granite thickens from about 1.5 to 3.5 km from the footwall of Argentat fault to the Pradines fault. East of it, the anomaly remains low, suggesting the presence of buried granite under the surface micaschists. Eastward, the anomaly increases as gneissic units come to the surface and decreases again under the influence of Ussel granite. West of the Millevaches massif, the anomaly (i) increases because of the dense (2800 kg/m^3) high pressure rocks that crop out in the Uzerche synform, and (ii) decreases in the Tulle antiform because of a 4-km-thick two-mica leucogranite occurrence (Roig et al., 1998 and Bellot, 2001).

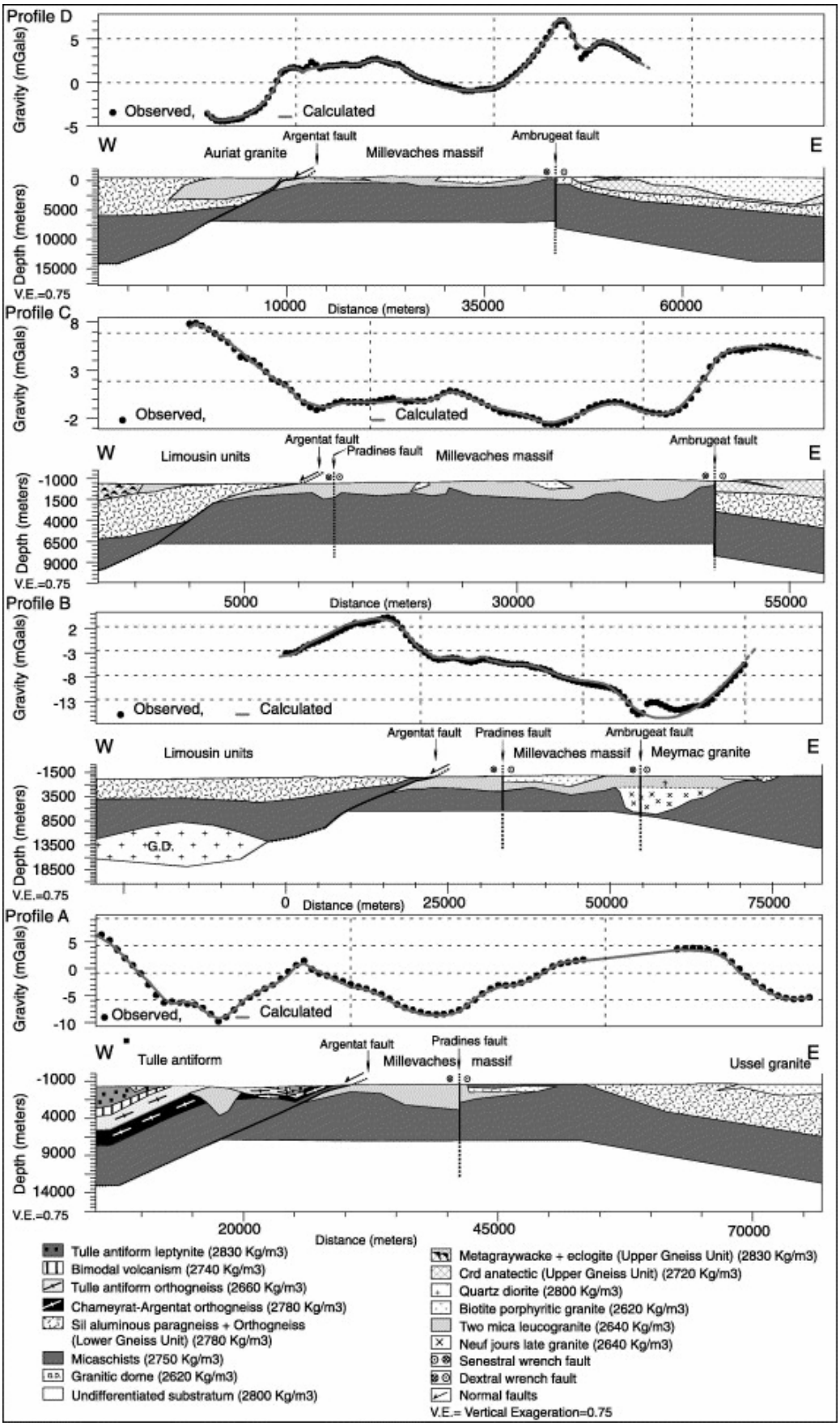

Fig. 11. Direct 2D gravity modelling through the Millevaches massif along E–W cross-sections from south to north (see location on Fig. 10).

Profile B (Fig. 11): The granite can be described as a laccolith 3–3.5-km-thick. As already mentioned in Gébelin et al. (2004), the eastern extremity of the Millevaches massif is associated with a high negative gravity anomaly reflecting late buried granite (Neuf Jours granite) (Burnol et al., 1980) and not the Millevaches massif eastward extension (Stussi and Cuney, 1990). In the west part, the occurrence of granite in the Argentat fault footwall is essential to fit the Bouguer anomaly. West of the Millevaches, the anomaly becomes positive due to the effect of the outcropping dense Bt/Sil gneisses then decreases, in relation with the deep granitic dome that was imaged at about 8 to 15–20 km depth in the Laurieras deep seismic profile (Bitri et al., 1999; Fig. 10).

Profile C (Fig. 11): It provides no information that has not already described in previous work (Gébelin et al., 2004) except the occurrence of granite in the Argentat fault footwall.

Profile D (Fig. 11): The Millevaches is modelled as a 1–2-km-thick laccolith. West of the Argentat fault, the Auriat granite is modelled as a 3.5-km-thick pluton. East of the Millevaches massif, the dense gneissic units induce a positive gravity anomaly, which then decreases toward the Guéret granite.

All these gravity profiles allow us to confirm previous work (Gébelin et al., 2004) that modelled the Millevaches massif as a laccolith. In addition, those 2D gravity models show the systematic occurrence of granite in the footwall of the Argentat fault and an increased thickness of granite under the Pradines fault. They reveal, east of the Pradines fault, the presence under the micaschists of a thin layer of buried granite rooted to the Pradines fault, and not extending to the southern continuity of the Ambrugeat fault. Moreover, the difference in thickness between the Auriat and Tulle antiform granites and the Millevaches granites strengthens the idea of an uplift of the Millevaches block along the footwall of the Argentat normal fault.

To compare the Millevaches massif with other granitic plutons and investigate relationships with surrounding terrains, we present two regional sub-meridian gravity profiles (E and F) orthogonal to the four previous A, B, C and D sections. All profiles are modelled in geometrical coherence with each other.

Profile E (Fig. 12): The central part exhibits a strong positive anomaly that does not fit with the low densities Guéret granite (about 2620 kg/m^3). This implies very thin Guéret granite (not more than a few hundred metres) as shown by the occurrence of cordierite anatexite outcrops in the central part. To fit the anomaly in amplitude and wavelength, we have also added between 4 and 5 km depth a very dense (3100 kg/m^3) body, below the Guéret massif. We interpret this dense body, about 1 km thick, to be high-pressure dense rocks of the Upper Gneiss Unit. To the north of Guéret, in agreement with previous modelling (Dumas et al., 1990), the Crozant granite is modelled as a 2-km-thick pluton rooted southwards into the Marche fault plane. South of the Guéret massif, the Millevaches massif thickens from about 1 to 4 km as shown by the slowly decreasing gravity anomaly. At the SSE end of the profile, the gravity anomaly decreases under the influence of the Neuf Jours granite (Burnol et al., 1980), and then increases as dense metamorphic para-autochthonous units come to the surface.

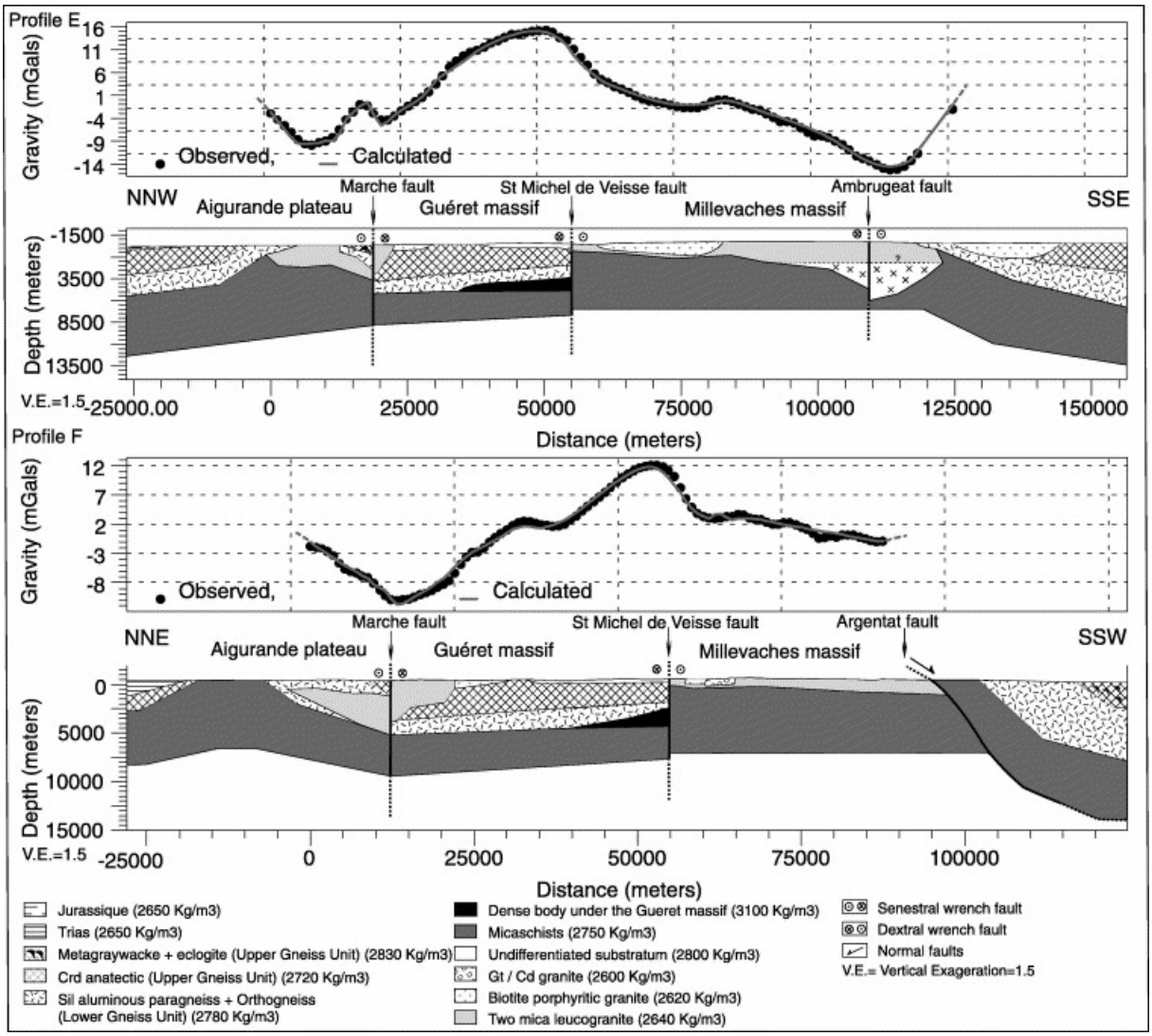

Fig. 12. N–S regional direct 2D gravity modelling from the Aigurande plateau to the Millevaches massif. These two profiles crosscut the four previous A, B, C and D models with a geometrical coherence with them. (See location on Fig. 10).

Profile F (Fig. 12): It crosscuts C, D and E profiles and allows us to confirm the overall geometries of the surface and deep units. To the north, leucogranite plutons are deep-rooted into the Marche fault. To the north, the occurrence of such tabular shape granite rooted at depth is attested by the persistence of the gravity low even if denser gneisses are mapped at surface. To the south, the profile confirms the low thickness of granite in the northwestern part of the Millevaches massif.

The gravity study at the Limousin regional scale reveals flat-shaped granites that do not invoke the classical diapiric model (Lameyre, 1982, Duthou and Floc'h, 1989 and Rolin and Colchen, 2001). Unlike Millevaches and Guéret granites, the Aigurande plateau two-mica leucogranites show a high negative anomaly directly below the Marche fault. As the other Limousin granites, but more particularly for the Guéret paradoxical granites that appear very large on the geological map, represent in cross-section very thin layers.

6. Discussion

6.1. Relationships between AMS fabric and regional structures

The magnetic foliation pattern presents a high dip in the north and east boundaries of the massif and in the Pradines fault, whereas it shows a general sub-horizontal dip on both sides of it. Most of the magnetic lineations are sub-horizontal; none of them present a steep plunge, which might suggest a rooting of Millevaches granites. The horizontal magnetic foliations and lineations are therefore consistent with the thin laccolith model.

It is worth noting that prolate type magnetic ellipsoids characterize the Millevaches massif. The magnetic lineations are better defined than the magnetic foliations (solid arrows in Fig. 8 and Table 1). Throughout the Millevaches massif, the magnetic lineation trend exhibits a sigmoïdal pattern, N–S in the inner part of the Pradines fault and NW–SE on both sides of it, that are consistent with a dextral wrench component. This N–S direction, parallel to the Pradines fault corresponds to the general trend of the Millevaches massif. Sometimes, this regular lineation pattern is not evident (Fig. 8). In fact, the most lineations derived from this pattern are statistically less reliable because the foliation is better defined at these sites (open arrows in Fig. 8 and Table 1).

Microscopic observations show that samples from two-mica leucogranites or porphyritic biotite granites exhibit purely magmatic structures rather than deformation in the Pradines fault area. The magmatic origin is also characterised by the weak magnetic anisotropy degree (P<10%). Subsolidus structures, considered to be records of the deformation in the continuum of the magmatic stage, are observed on both sides of the Pradines fault. All these observations are also in agreement with the high-temperature recurrent quartz microstructures and the typical C–S structures indicating a dextral shearing sense recorded in the Pradines mylonitic two-mica leucogranites (Gébelin et al., 2004). Many observations attest to the important role played by the Pradines fault in the Millevaches magma emplacement: (i) its N–S orientation parallel to the general trend of the Millevaches massif, (ii) its large thickness (5 km), (iii) the high temperature deformation of mylonitic microstructures, (iv) the occurrence of vertically-foliated xenoliths (Fig. 1), (v) the bed by bed partial melting suffered by the micaschists during a dextral wrench movement (Fig. 2b). The plot of the shape (T) and anisotropy degree (P) parameters of two-mica leucogranites and porphyritic biotite granites show an undifferentiated repartition of the linear (prolate) and planar (oblate) shapes (Fig. 6) implying they are emplaced in the same tectonic context associated with the activity of the Pradines fault. This is in agreement with the structural observations of Stussi and Cuney (1990) but call into question the separation of the two types of granites based on Rb/Sr isotopic data.

In the northern part of the massif, the magnetic lineations and foliations become progressively parallel to the St Michel de Veisse dextral wrench fault (Fig. 8 and Fig. 9). This fault seems to have influenced the granite magnetic fabric pattern. Field observations and AMS data show the foliations and lineations follow the edge of the pluton and become N–S along the Felletin ductile dextral wrench fault (Fig. 9). This suggests that Pradines but also St Michel de Veisse, Felletin and Ambrugeat faults control the magma emplacement. Therefore, it seems that the Millevaches granites emplacement was more influenced by the wrench tectonic developed during late-Variscan times (Arthaud and Matte, 1977) than the Carboniferous post-collisional thinning regional tectonic coeval also with a NW–SE ductile deformation, which is illustrated by general E–W to NW–SE orientated magnetic lineations (Faure, 1995 and Talbot et al., 2004).

6.2. Emplacement model

As a working hypothesis, we suggest that the large Pradines fault might constitute a feeding zone for the Millevaches granites. Hence, combining field observations, AMS data, gravity models and seismic profiles, we propose two general E–W geological cross-sections on which the Millevaches leucogranites appear as a horizontal layer fed by vertical conduit (profiles A and B; Fig. 13). How can one explain the rapid transition from a vertical foliation in the 5-km-wide Pradines fault to sub horizontal foliation elsewhere (Fig. 13B)?

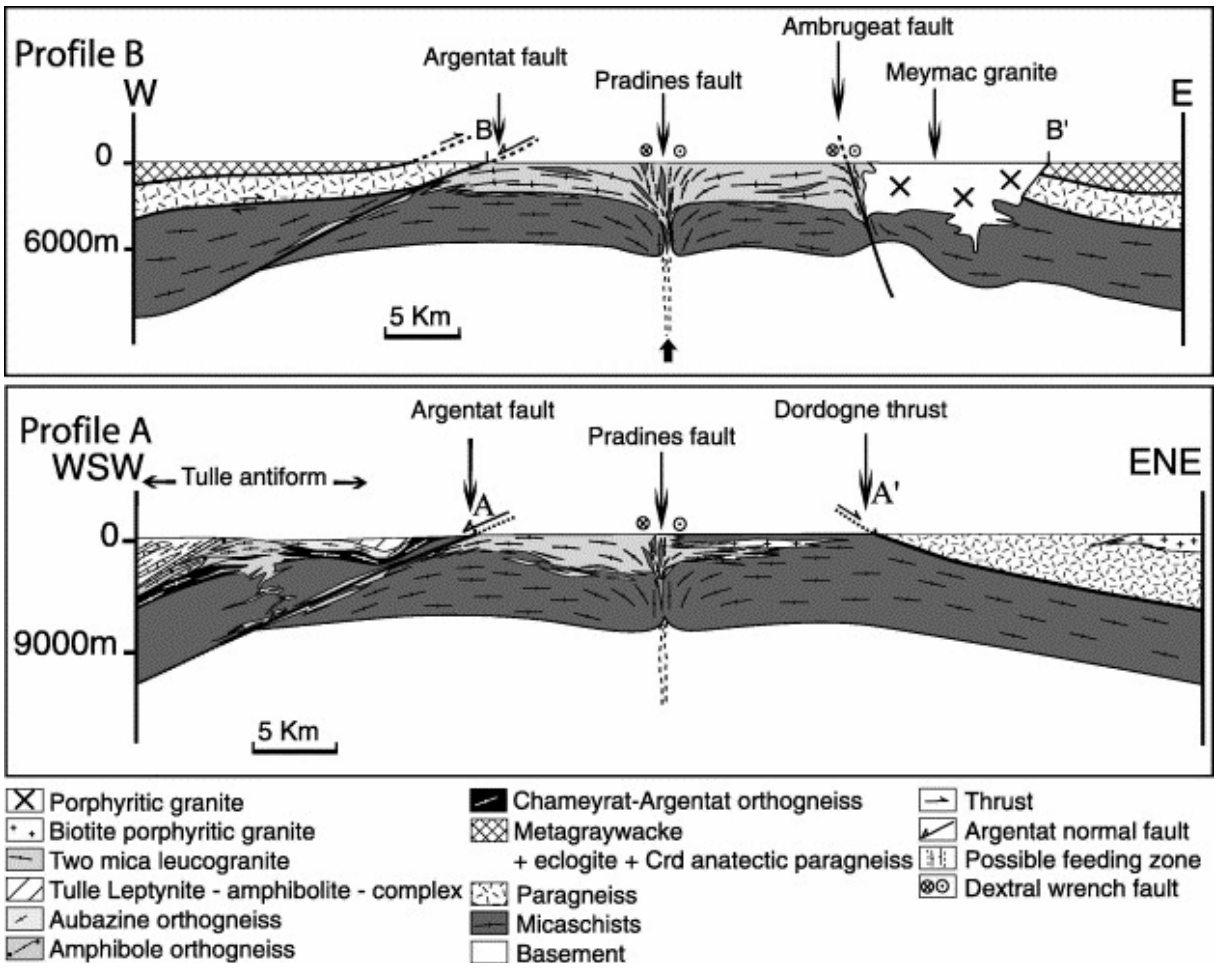

Fig. 13. Sketch geological cross-sections through the Millevaches granitic massif along profiles A and B, built from field observations, seismic profiles, AMS and gravity data. (See location on Fig. 10.)

In the present state of our knowledge, we propose that the Pradines dextral wrench fault deformed a crust already horizontally structured (Fig. 14a) by the Variscan crustal stacking (Matte, 1986). This accident of at least crustal scale, focuses the magma at depth, which ascends through the vertical conduit towards the middle crust (Fig. 14a). Magmas are then trapped and channelled in the previously-formed flat-lying micaschist foliation, which constitutes a major mechanical anisotropy of the middle crust (Fig. 14a and b). Synkinematic plutons emplaced by the dextral wrenching Pradines fault record N–S-trending deformation trajectories in the Pradines fault and NW–SE on both sides of it (Fig. 14b). The magma rising towards the roof of the laccolith induces an oblate coaxial deformation accommodated by flat-lying normal faults, such as the Argentat fault (Fig. 13).

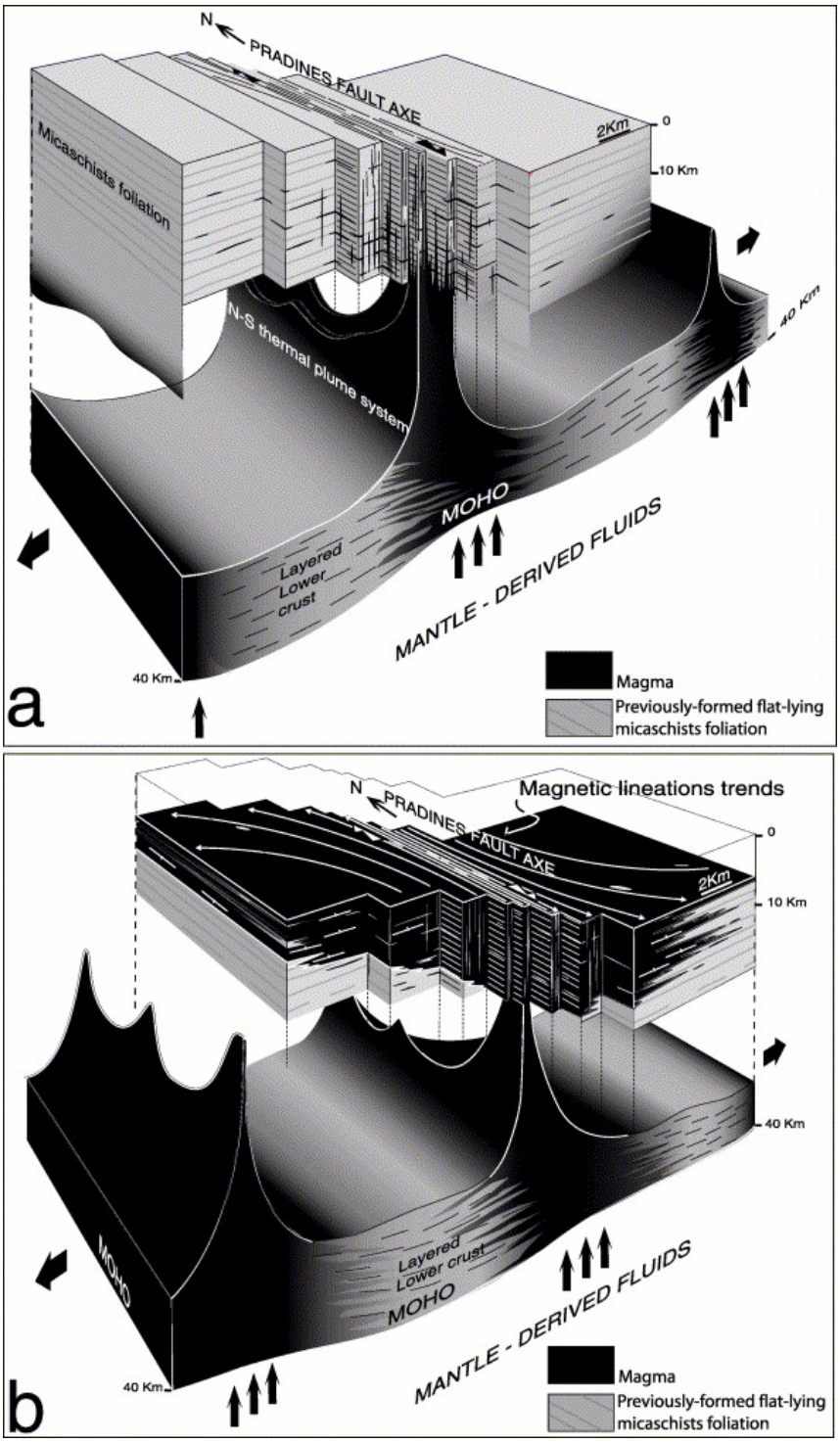

Fig. 14. Emplacement model for the Millevaches granites. (a) First stage of granite emplacement. (i) Pradines dextral wrench fault affects a crust already horizontally structured. (ii) Magma ascent proceeds through vertical narrow ducts by successive injections along the NS-oriented principal axis of the Pradines fault. (iii) Magmas are trapped and channelled in a major mechanical anisotropy of the middle crust (the previously-formed flat-lying micaschist foliation). (iv) Mantle-derived fluids underplating could have participate to partial melting of the metasedimentary lower crust and genesis of magmas (Williamson et al., 1996). (b) Final stage of magma emplacement. The migration of magma through the sub horizontal micaschist foliation reached its maximum, forming the Millevaches laccolith. Synkinematic plutons emplaced in the dextral wrenching Pradines fault record N–S-trending deformation trajectories (long white arrows) in the Pradines fault and NW–SE on both sides of it.

This temporary emplacement model, already proposed by Pollard and Johnson, 1973, Jackson and Pollard, 1988 and Corry, 1988 through quantitative studies of the laccoliths emplacement in the crust, poses nevertheless many questions. First, there is no field evidence of vertical flow at the surface, where the tectonic dextral transcurrent movement prevails. Second, there is no large negative gravity anomaly associated with the Pradines fault. Third, could the Argentat fault, but also the other wrench faults, play a feeding zone role? Fourth, what are the source and nature of heat generating such important quantity of magma? In the proposed model, we might suggest that the high-dipping lineations related to the magma ascent could have disappeared during the granite emplacement by the Pradines dextral wrench mechanism. The weak negative anomaly underneath the Pradines fault could be explained by vertical narrow ducts that disappear after the passage of magma that did not crystallize in the conduit. Magma ascent might proceed by successive injections along the NS-oriented principal axis of the Pradines fault (Fig. 14b) explaining the composite geometry (many small laccoliths) of the Millevaches massif. The other faults could also play a feeding zone role but none of them has the same large extent as the Pradines fault! Moreover, the occurrence under the micaschists of a thin layer of buried granite rooted to the Pradines fault, and not extending to the south continuity of the Ambrugeat fault (Fig. 11 and Fig. 13), indicates that this fault does not constitute a feeding zone. By comparison with Millevaches magmas genesis model proposed by Williamson et al. (1996), we suggest the lower crust anatexis and localisation of magma chambers could be due to underplating that has caused flushing of the lower crust by mantle-derived fluids inducing partial melting of the metasedimentary lower crust (Fig. 14). Nevertheless, many mechanisms can participate in the magma genesis and our study does not allow us to answer all the questions.

7. Conclusions

The large N–S-trending granitic complex of the Millevaches affected by dextral wrench faults was emplaced at the end of the Variscan orogeny within a strike-slip tectonic context. AMS helps to clarify the impact of wrench faults on the granites internal fabric. Finally, the gravity modelling and the structural study, thanks to the field observations and AMS investigation, allow a better understanding of the context of magma emplacement. Through the gravity modelling, the Millevaches granites appear as a thin horizontal layer, 1–4 km thick, from north to south. The granite thickness appears more important in the footwall of the Argentat fault and along the Pradines fault. The thick NS Pradines (5 km) shear zone with related high temperature mylonites is interpreted as a possible feeding zone for the Millevaches magmas. It played an important role in the Millevaches granites internal fabric. This assumption is supported by the magnetic lineation that reveals two main trends: a N–S direction characterized by pre-full crystallization microstructures in the Pradines fault zone and a predominant NW–SE orientation distinguished by pre-full crystallization and solid-state flow microstructures on either side of the central Pradines fault zone. Throughout the massif, the magnetic lineation path has a sigmoid shape pattern that is in agreement with a dextral sense of the Pradines shear zone. As already noticed in the field, the magnetic foliation pattern shows a high dip in the Pradines fault and a general sub horizontal dip on both sides of the N–S Pradines dextral wrench fault.

At the regional scale, the prolate type ellipsoid is dominant and confirms the validity of the magnetic lineation path. Therefore, the emplacement of Millevaches massif is dominated by the influence of a dextral strike-slip tectonic context rather than the late-orogenic extension event (Faure, 1995 and Talbot et al., 2004). Finally, gravity modelling and AMS results best

explain the paradox of the large surface outcrop of granites at variance with their small thickness or abundance in vertical section.

We thank C. Truffert and J.Y. Roig for fruitful discussions concerning the Argentat seismic profile interpretation as well as on the geology of nearby areas. We are pleased to thank M. Cuney for letting us share his experience of the Millevaches granites. A. Delplanque is also warmly thanked for providing support in the 3D drawing. Gravity modelling and geophysical maps were produced using Geosoft/GM-SYS software. The authors wish to thank K. Benn and J. Hippertt for constructive comments and reviews and David Mainprice for English editing.

References

Arthaud and Matte, 1977 F. Arthaud and P. Matte, Late Paleozoic strike-slip faulting in Southern Europe and Northern Africa: results of a right lateral shear zone between the Appalachians and the Urals, *Geological Society of America Bulletin* **88** (1977), pp. 1305–1320.

Augay, 1979 Augay, J.F., 1979. Les leucogranites et monzogranites de la région d'Eymoutiers–Peyrat le Château (Massif du Millevaches, Massif Central Français). Gisement et pétrologie. Unpublished doctoral dissertation, University of Lyon I, Lyon.

Bellot, 2001 Bellot, J.Ph., 2001. La structure de la croûte varisque du Sud-Limousin (Massif central français) et ses relations avec les minéralisations aurifères tardi-orogéniques: apport des données géologiques, gitologiques, géophysiques et de la modélisation 3D. Thèse de Doctorat de l'Université Montpellier II.

Bingham, 1964 Bingham, C., 1964. Distribution on a sphere and on the projective plane. PhD thesis, Yale University.

Bitri et al., 1999 A. Bitri, C. Truffert, J.-P. Bellot, V. Bouchot, P. Ledru, J.-P. Milesi and J.-Y. Roig, Imagerie des paléochamps hydrothermaux As–Au–Sb d'échelle crustale et des pièges associés dans la chaîne varisque: sismique réflexion verticale (GéoFrance3D: Massif central français), *Comptes Rendus de l'Académie des Sciences, Paris* **329** (1999), pp. 771–777.

Blumenfeld et al., 1986 P. Blumenfeld, D. Mainprice and J.-L. Bouchez, C-slip in quartz from subsolidus deformed granite, *Tectonophysics* **127** (1986), pp. 97–115.

Brown and Solar, 1998 M. Brown and G.S. Solar, Granite ascent and emplacement during contractional deformation in convergent orogens, *Journal of Structural Geology* **20** (1998), pp. 1365–1393.

Burnol et al., 1980 L. Burnol, Y. Peronne and H. Vaucorbeil, La coupole cachée de leucogranite de Neuf-Jours (Corrèze) et les minéralisations en tungstène associées, *Chronique Recherche Minière* **455** (1980), pp. 93–116.

Colchen and Rolin, 1996 Colchen, M., Rolin, P., 1996. Le Complexe des Essarts-Mervent dans la transversale vendeenne de la chaine hercynienne. Essarts-Mervent Complex in the

Vendee transverse of the Hercynian Geosyncline. Réunion Annuelle des Sciences de la Terre 7, 51pp.

Corry, 1988 Corry, C.E., 1988. Laccoliths; mechanics of emplacement and growth. Geological Society of America, Special Paper 220, 110pp.

Courrioux, 1983 G. Courrioux, Exemple de mise en place d'un leucogranite pendant le fonctionnement d'une zone de cisaillement: le granite hercynien de Puentedeume (Galice, Espagne), *Bulletin de la Société géologique de France* **125** (1983), pp. 301–307.

Cuney and Stussi, 1989 Cuney, M., Stussi, J.M., 1989. Synthèse géochimique sur les granites du Millevaches. Détermination de leur potentialité uranifère. Rapport au CEA, dont une carte géochimique en couleur du Millevaches au 1/100,000, 64pp.+annexes.

Cuney et al., 1990 M. Cuney, M. Friedrich, P. Blumenfeld, A. Bourguignon, M.-C. Boiron, J.-L. Vigneresse and B. Poty, Metallogenesis in the French part of the Variscan orogen. Part I: U preconcentrations in pre-Variscan and Variscan formations—a comparison with Sn, W and Au, *Tectonophysics* **177** (1990), pp. 39–57.

Downes et al., 1997 H. Downes, A. Shaw, B.J. Williamson and M.F. Thirlwall, Hercynian granodiorites and monzogranites, Massif Central, France, *Chemical Geology* **136** (1997) (1–2), pp. 99–122.

Dumas et al., 1990 E. Dumas, M. Faure and J. Pons, L'architecture des plutons leucogranitiques du plateau d'Aigurande et l'amincissement crustal tardi-varisque, *Comptes Rendus de l'Académie des Sciences, Paris II* **310** (1990), pp. 1533–1539.

Duthou and Floc'h, 1989 J.L. Duthou and J.P. Floc'h, Evolution tectonométamorphique du Massif Central. Réunion Extraordinaire de la Société géologique de France, *Bulletin de la Société géologique de France* **4** (1989), pp. 667–693.

Eggleton and Buseck, 1980 R.A. Eggleton and P.R. Buseck, The orthoclase–microcline inversion: a high-resolution transmission electron microscope study and strain analysis, *Contribution to Mineralogy and Petrology* **74** (1980), pp. 123–133.

Faure, 1989 M. Faure, L'amincissement crustal de la chaîne varisque à partir de la déformation ductile des leucogranites du Limousin, *Comptes Rendus de l'Académie des Sciences, Paris II* **309** (1989), pp. 1839–1845.

Faure, 1995 M. Faure, Late orogenic Carboniferous extensions in the Variscan French Massif Central, *Tectonics* **14** (1995), pp. 132–153.

Faure and Pons, 1991 M. Faure and J. Pons, Crustal thinning recorded by the shape of the Namurian–Westphalian leucogranite in the Variscan belt of the Northwest Massif Central, France, *Geology* **19** (1991), pp. 730–733.

Floc'h, 1983 Floc'h, J.-P., 1983. La série métamorphique du Limousin central: une traverse de la branche ligérienne de l'orogène varisque, de l'Aquitaine à la zone broyée d'Argentat (Massif Central Français). Thèse d'Etat, Limoges, 445pp.

Gapais and Barbarin, 1986 D. Gapais and B. Barbarin, Quartz fabric transition in a cooling syntectonic granite (Hermitage massif, France), *Tectonophysics* **125** (1986) (4), pp. 357–370.

Gébelin et al., 2004 A. Gébelin, G. Martelet, M. Brunel, M. Faure and P. Rossi, Late Hercynian leucogranites modelling as deduced from new gravity data: the example of the Millevaches massif, Massif Central, France, *Bulletin de la Société géologique de France* **175** (2004) (3), pp. 239–248.

Gower and Simpson, 1992 R.J.W. Gower and C. Simpson, Phase boundary mobility in naturally deformed, high-grade quartzofeldspathic rocks: evidence for diffusional creep, *Journal of Structural Geology* **14** (1992), pp. 301–313.

Guineberteau et al., 1987 B. Guineberteau, J.-L. Bouchez and J.-L. Vigneresse, The Mortagne granite pluton (France) emplaced by pull-apart along a shear zone: structural and gravimetric arguments and regional implication, *Geological Society of America Bulletin* **99** (1987), pp. 763–770.

Hargraves et al., 1991 R.B. Hargraves, D. Johnson and C.Y. Chan, Distribution anisotropy; the cause of AMS in igneous rocks?, *Geophysical Research Letters* **18** (1991) (12), pp. 2193–2196.

Hibbard, 1987 M.J. Hibbard, Deformation of incompletely crystallized magma systems: granitic gneisses and their tectonic implications, *Journal of Geology* **95** (1987), pp. 543–561.

Hrouda, 1982 F. Hrouda, Magnetic anisotropy of rocks and its application in geology and geophysics, *Geophysical Surveys* **5** (1982), pp. 37–82.

Hutton, 1982 D.H.W. Hutton, A tectonic model for the emplacement of the Main Donegal granite, NW Ireland, *Journal Geological Society of London* **139** (1982), pp. 615–631.

Ingram and Hutton, 1994 G.M. Ingram and D.H.W. Hutton, The Great Tonalite Sill: emplacement into a contractional shear zone and implications for Late Cretaceous to early Eocene tectonics in southeastern Alaska and British Columbia, *Geological Society of America Bulletin* **106** (1994), pp. 715–728.

Jackson and Pollard, 1988 M.D. Jackson and D.P. Pollard, The laccolith-stock controversy: new results from the southern Henry Mountains, Utah, *Geological Society of America Bulletin* **100** (1988), pp. 117–139.

Jelinek, 1978 V. Jelinek, Statistical processing of anisotropy of magnetic susceptibility measured on groups of specimens, *Studia Geophyzika et Geodetika* **22** (1978), pp. 50–62.

Jelinek, 1981 V. Jelinek, Characterization of the magnetic fabric of rocks, *Tectonophysics* **79** (1981), pp. 563–567.

Jessel, 1987 M.W. Jessel, Grain-boundary migration microstructures in a naturally deformed quartzite, *Journal of Structural Geology* **9** (1987), pp. 1007–1014.

Jover, 1986 Jover, O., 1986. Les massifs granitiques de Guéret et du nord-Millevaches. Analyse structurale et modèle de mise en place (Massif Central Français). Thèse de doctorat, Nantes, 233pp.

Koukouvelas et al., 2002 I. Koukouvelas, G. Pe-Piper and D.J.W. Piper, The role of dextral transpressional faulting in the evolution of an early Carboniferous mafic–felsic plutonic and volcanic complex: Cobequid Highlands, Nova Scotia, Canada, *Tectonophysics* **348** (2002), pp. 219–246.

Lameyre, 1982 J. Lameyre, Contribution à la géologie du Limousin: arguments pour des fenêtres ouvertes dans un grand charriage par des diapirs leucogranitiques, *Comptes Rendus de l'Académie des Sciences* **2949** (1982), pp. 1237–1240.

Ledru et al., 1989 P. Ledru, J.-M. Lardeaux, D. Santallier, A. Autran, J.-M. Quenardel and J.-P. Floc'h, Où sont les nappes dans le Massif central français?, *Bulletin de la Société géologique de France* **8** (1989), pp. 605–618.

Mainprice and Bouchez, 1986 D. Mainprice and J.-L. Bouchez, Dominant *c* slip in naturally deformed quartz: implications for dramatic plastic softening at high temperature, *Geology* **14** (1986), pp. 819–822.

Matte, 1986 P. Matte, Tectonics and plate tectonics model for the Variscan belt of Europe, *Tectonophysics* **126** (1986), pp. 329–374.

Matte, 1998 P. Matte, Continental subduction and exhumation of HP rocks in Paleozoic belts: Uralides and Varicides. Special Issue Tectonics and General History of Phanerozoic orogens, *Geological Society Sweden (G.F.F.)* **120** (1998), pp. 209–222.

Mezure, 1980 Mezure, J.-F., 1980. Etude structurale des granites d'Egletons, Meymac et Ussel (Nord). Contribution à l'estimation quantitative de la déformation. Pétrographie et géochimie. Thesis of speciality, Univ. Clermont-Ferrant, 191pp.

Monier, 1980 Monier, G., 1980. Pétrologie des granitoïdes du Sud Millevaches (Massif Central Français). Minéralogie, géochimie, géochronologie. Thèse 3ème Cycle, Université de Clermont II, 288pp.

Pollard and Johnson, 1973 D.D. Pollard and A.M. Johnson, Mechanics of growth of some laccolithic intrusions in the Henry Mountains, Utah, II—bending and failure of overburden layers and sill formation, *Tectonophysics* **18** (1973), pp. 318–354.

Roig et al., 1998 J.-Y. Roig, M. Faure and C. Truffert, Folding and granite emplacement inferred from structural, strain, TEM, and gravimetric analyses: the case study of the Tulle antiform, SO French Massif Central, *Journal of Structural Geology* **20** (1998) (9–10), pp. 1169–1189.

Rolin and Colchen, 2001 P. Rolin and M. Colchen, Carte structurale du socle Varisque Vendée-Seuildu Poitou-Limousin, *Géologie de la France* **1–2** (2001), pp. 3–6.

Speer et al., 1994 J.A. Speer, H.Y. McSween and A.E. Gates, Generation, segregation, ascent, and emplacement of Alleghanian plutons in the Southern Appalachians, *Journal of Geology* **102** (1994), pp. 249–267.

Stussi and Cuney, 1990 J.M. Stussi and M. Cuney, Granites et leucogranites des massifs de Peret Bel Air et Egletons, *Rapport sur les travaux réalisés dans le cadre du Contrat* (1990), pp. MC/15/142–CEA/DAMN-CREGU.

Talbot et al., 2004 J.Y. Talbot, G. Martelet, G. Courrioux, Y. Chen and M. Faure, Emplacement in an extensional setting of the Mont Lozère–Borne granitic complex (SE France) inferred from comprehensive AMS, structural and gravity studies, *Journal of Structural Geology* **26** (2004), pp. 11–28.

Tikoff and Saint Blanquat, 1997 B. Tikoff and M. Saint Blanquat, Transpressional shearing and strike-slip partitioning in the late Cretaceous Sierra Nevada magmatic arc, California, *Tectonics* **16** (1997) (442), p. 459.

Vidal, 1973 P. Vidal, Premières données géochronologiques sur les granites hercyniens du sud du Massif Armoricain, *Bulletin de la Société géologique de France* **7** (1973), pp. 239–245.

Williamson et al., 1996 B.J. Williamson, A. Shaw, H. Downes and M.F. Thirwall, Geochemical constraints on the genesis of Hercynian two-mica leucogranites from the Massif Central, France, *Chemical Geology* **127** (1996), pp. 25–42.